

Air Force Institute of Technology

**AFIT Scholar**

---

Theses and Dissertations

Student Graduate Works

---

3-2005

## Efficient Electromagnetic material Characterization Via 2-D Rectangular Waveguide Reduction

Derek R. Dwyer

Follow this and additional works at: <https://scholar.afit.edu/etd>



Part of the [Electromagnetics and Photonics Commons](#)

---

### Recommended Citation

Dwyer, Derek R., "Efficient Electromagnetic material Characterization Via 2-D Rectangular Waveguide Reduction" (2005). *Theses and Dissertations*. 3861.

<https://scholar.afit.edu/etd/3861>

This Thesis is brought to you for free and open access by the Student Graduate Works at AFIT Scholar. It has been accepted for inclusion in Theses and Dissertations by an authorized administrator of AFIT Scholar. For more information, please contact [AFIT.ENWL.Repository@us.af.mil](mailto:AFIT.ENWL.Repository@us.af.mil).



**EFFICIENT ELECTROMAGNETIC MATERIAL CHARACTERIZATION VIA  
2-D RECTANGULAR WAVEGUIDE REDUCTION**

THESIS

Derek R. Dwyer, First Lieutenant, USAF

AFIT/GE/ENG/05-01

**DEPARTMENT OF THE AIR FORCE  
AIR UNIVERSITY  
AIR FORCE INSTITUTE OF TECHNOLOGY**

**Wright-Patterson Air Force Base, Ohio**

APPROVED FOR PUBLIC RELEASE; DISTRIBUTION UNLIMITED.

The views expressed in this thesis are those of the author and do not reflect the official policy or position of the United States Air Force, Department of Defense, or the United States Government.

AFIT/GE/ENG/05-01

EFFICIENT ELECTROMAGNETIC MATERIAL CHARACTERIZATION VIA 2-D  
RECTANGULAR WAVEGUIDE REDUCTION  
THESIS

Presented to the Faculty  
Department of Electrical and Computer Engineering  
Graduate School of Engineering and Management  
Air Force Institute of Technology  
Air University  
Air Education and Training Command  
In Partial Fulfillment of the Requirements for the  
Degree of Master of Science in Electrical Engineering

Derek R. Dwyer, B.S.E.E.

First Lieutenant, USAF

March 2005

APPROVED FOR PUBLIC RELEASE; DISTRIBUTION UNLIMITED


AFIT/GE/ENG/05-01

EFFICIENT ELECTROMAGNETIC MATERIAL CHARACTERIZATION VIA 2-D  
RECTANGULAR WAVEGUIDE REDUCTION

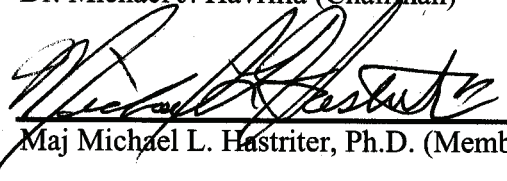
Derek R. Dwyer, B.S.E.E

First Lieutenant, USAF

Approved:

  
\_\_\_\_\_  
Dr. Michael J. Havrilla (Chairman)

16 Mar 05  
Date

  
\_\_\_\_\_  
Maj Michael L. Hastriter, Ph.D. (Member)

15 Mar 05  
Date

  
\_\_\_\_\_  
Dr. William P. Baker (Member)

15 Mar 05  
Date

### **Abstract**

A new, low-frequency, rectangular waveguide-based electromagnetic material characterization technique is developed that will reduce the test sample size in two dimensions realizing up to 75 percent reduction in sample cross-sectional area. To achieve this, custom made, reduced aperture, sample holder flanges were used that reduce the waveguide's excessive cross-sectional dimensions, resulting in reduced sample fabrication costs. Additionally, MatLab<sup>®</sup> code was developed to implement the rigorously derived modal-analysis solution that accommodates induced, higher-order transverse electric and transverse magnetic modes and accurately extract the reduced test sample's constitutive parameters.

Experimental results using various test samples are compared to known, full-aperture measurements for both the reduced aperture waveguide configurations to verify the theoretical analysis. A differential error analysis is also performed for each configuration in an attempt to estimate the error associated with test sample thickness, aperture dimensions, and sample placement uncertainties.

## **Acknowledgments**

I would like to thank Dr Havrilla for his unmatched patience and kindness throughout the rigorous and painful 18-month low-observables curriculum. His mastery of electromagnetics, both academically and professionally, combined with a profound talent and desire to teach has made his lectures and mentoring the true “jewel” of my AFIT experience. I would also like to thank Dr George “Bob” Simpson and AFRL/SNS for sponsoring my research. A great amount of gratitude is extended to Capt Sean Dorey for providing his 1-D waveguide reduction code as a “spring-board” for the 2-D waveguide reduction code developed in this effort. Additionally, I would like to thank Rodney George, and the rest of the AFRL sensors team that were involved in machining the various fixtures designed for this thesis.

Derek Dwyer

## Table of Contents

1. Introduction.....	1-1
1.1 Problem Statement .....	1-3
1.2 Limitations .....	1-4
1.3 Scope .....	1-4
1.4 Thesis Organization .....	1-5
2. Background.....	2-1
2.1 TE and TM Modes of a Rectangular Waveguide.....	2-1
2.1.1 Maxwell’s Equations .....	2-3
2.1.2 Helmholtz Wave Equation .....	2-5
2.1.3 Helmholtz Wave Equation Applied to Rectangular Waveguide .....	2-6
2.1.4 Separation of Variables .....	2-8
2.1.5 Application of Waveguide’s Boundary Conditions.....	2-11
2.1.6 Order of Modes Determined by Cut-off Frequency .....	2-16
2.2 Wave Transmission Matrices (A-Parameters).....	2-18
2.2.1 A-parameters for Single Layer Configuration .....	2-19
2.2.2 A-Parameters for Multiple Layer Configuration. ....	2-22
2.3 Summary .....	2-23



3.	Methodology.....	3-1
3.1	Field Expansions .....	3-2
3.1.1	2-D Stepped-Waveguide Geometry.....	3-2
3.1.2	Derivation of Higher-Order Scattered Fields.....	3-4
3.1.3	Mode Orthogonality .....	3-8
3.1.4	Field Expansions in Waveguide Regions.....	3-10
3.1.5	Field Expansions in Sample Region.....	3-13
3.2	Satisfying Boundary Conditions .....	3-15
3.3	Testing with Integral Operators.....	3-19
3.4	Material Parameter Extraction.....	3-23
3.5	Summary.....	3-24
4.	Results and Error Analysis .....	4-1
4.1	Reduced Aperture Experimental Setup.....	4-2
4.2	Error Analysis .....	4-4
4.3	Reduced Aperture Results for Acrylic Test Sample .....	4-6
4.4	Reduced Aperture Results for MRAM Test Sample.....	4-9
4.5	Summary .....	4-14
5.	Conclusion and Recommendations.....	5-1
5.1	Future Research.....	5-2

Appendix A	Proofs of Inner-Products .....	A-1
A.1	Proof for $C_{lp}$ .....	A-1
A.2	Proof for $C_{ll}$ .....	A-2
A.3	Proof for $Q_{lp}$ .....	A-2
A.4	Proof for $P_{lp}$ .....	A-3
A.5	Proof for $D_{lp}$ .....	A-4
A.6	Proof for $F_{lp}$ .....	A-7
Appendix B	Sample Holder Drawings .....	B-1
B.1	25% Waveguide Reduction Sample Holder/Flange.....	B-2
B.2	50% Waveguide Reduction Sample Holder/Flange.....	B-3
B.3	75% Waveguide Reduction Sample Holder/Flange.....	B-4
B.4	Other Equipment .....	B-5

## List of Figures

	Page
<b>Figure 2-1</b> Cross-sectional dimensions of the rectangular waveguide .....	2-2
<b>Figure 2-2</b> Layout of single layer material with reflected waves and transmitted waves .....	2-19
<b>Figure 2-3</b> Layout of Multiple Layer Configuration .....	2-22
<b>Figure 3-1</b> Cross-sectional view of 2-D stepped waveguide fixture looking at the $z = 0$ interface. Symbols $\vec{J}_s$ identify excited surface currents caused by the incident $TE_{10}$ wave. ....	3-3
<b>Figure 3-2</b> Top view of 2-D reduced aperture waveguide fixture having one unknown layer (i.e. center) and multiple known layers. This arrangement presents a generic view that encompasses all possible sample holder configurations. Sample holder width exaggerated to adequately detail sample region. Symbols $\vec{J}_s$ identify excited surface currents caused by incident $TE_{10}$ wave.....	3-3
<b>Figure 3-3</b> Side view of 2-D reduced aperture waveguide fixture having one unknown layer (i.e. center) and multiple known layers. ....	3-4

## List of Figures

	Page
<b>Figure 4-1.</b> Experimental setup showing the WR284 waveguide connected to an HP8510B Network Analyzer via coaxial cables. The reduced-aperture sample holder is mounted between the waveguide feeds using precision alignment pins. ....	4-3
<b>Figure 4-2</b> S-band reduced aperture sample holders. From left to right are: 25% (2.46"×1.16") reduced waveguide sample holder, 50% (2.01"×.95") reduced waveguide sample holder and the 75% (1.42"×.67") reduced waveguide sample holder. ....	4-3
<b>Figure 4-3.</b> Real permittivity for acrylic test sample mounted in the 2.46"×1.16", 25% reduction sample holder. Approximately 20 modes are required for convergence to the full-aperture baseline. ....	4-8
<b>Figure 4-4.</b> Real permittivity for acrylic test sample mounted in the 2.01"×.95", 50% reduction sample holder. Approximately 20 modes are required for convergence to the full-aperture baseline. ....	4-8
<b>Figure 4-5.</b> Real permittivity for acrylic test sample mounted in the 1.42"×.67", 75% reduction sample holder. Approximate 11% error caused by uncorrectable scratches and blemishes on sample's surface. ....	4-9
<b>Figure 4-6.</b> Permittivity of MRAM test sample mounted in 2.46"×1.16", 25% reduction sample holder. ....	4-11
<b>Figure 4-7.</b> Permeability of MRAM test sample mounted in 2.46"×1.16", 25% reduction sample holder. ....	4-11
<b>Figure 4-8.</b> Permittivity of MRAM test sample mounted in the 2.01"×.95", 50% reduction sample holder. ....	4-12
<b>Figure 4-9.</b> Permeability of MRAM test sample mounted in the 2.01"×.95", 50% reduction sample holder. ....	4-12
<b>Figure 4-10</b> Permittivity of MRAM test sample mounted in the 1.42"×.67", 75% reduction sample holder. ....	4-13
<b>Figure 4-11</b> Permeability of MRAM test sample mounted in the 1.42"×.67", 75% reduction sample holder. ....	4-13

# **EFFICIENT ELECTROMAGNETIC MATERIAL CHARACTERIZATION VIA 2-D RECTANGULAR WAVEGUIDE REDUCTION**

## ***1. Introduction***

The technique used to measure a material's constitutive parameters (complex permittivity & permeability) depends on many factors such as: frequency, sample size, temperature and sample fabrication requirements for example. The goal of the electromagnetic characterization technique is to effectively record the material's complex permittivity and permeability across a certain band of frequencies. Permittivity describes how susceptible a material is to becoming polarized when exposed to an external electric field. Similarly, permeability describes how susceptible a material is to becoming polarized when exposed to an external magnetic field. Both permittivity and permeability are complex quantities where the real part accounts for a material's ability to store energy and the imaginary part accounts for the material's loss mechanisms due to microscopic dampening forces.

Determining the constitutive parameters of lower-frequency materials using standard rectangular waveguide testing techniques [1]-[5] requires the test sample to completely fill the cross-sectional dimensions of the waveguide. To accommodate low frequencies, the test waveguide dimensions can be on the order of a meter or more. This implies the test sample's cross-sectional area must be large to completely fill the waveguide.

The resources required to manufacture such large test samples are costly, making the task of characterizing low-frequency electromagnetic materials expensive. Furthermore, machining and fitting large test samples into the waveguide can be extremely difficult as the samples can be thin and may require supporting structures to facilitate measurement (i.e. sandwich sample between known materials) so as to maintain the planar rigidity requirement [1]-[5]. Because material development is an iterative process, the cost, effort, and time needed to electromagnetically characterize low-frequency prototype materials can make the task exorbitantly expensive.

Recent efforts [10] to minimize the sample fabrication requirements of low-frequency material characterization using rectangular waveguides have yielded a method that allows the test waveguide to be reduced in width only, which makes the test sample size narrower, hence less cross-sectional surface area. The advantage of this technique is that it alleviates sample size requirements by utilizing a rigorous modal-analysis technique. However, a limitation of this technique is that the sample size is minimized in only one dimension (i.e. width), which still maintains somewhat of a burden on sample machining and expensive material resources. Other well-known approaches to address the sample size problem are the longitudinal section electric and longitudinal section magnetic methods [6],[7]. Although these approaches realize a reduced sample size, they require solving transcendental equations, have problems associating correct modes with the respective propagation constants, and can be very sensitive to the initial guess selection for the constitutive parameters.

This thesis proposes a technique that reduces the waveguide structure in two dimensions symmetric about the rectangular waveguide's transverse axes and solves for

the constitutive parameters via rigorous modal analysis and root searching algorithms. This technique will significantly reduce the expenditures and time associated with low-frequency material characterization.

### ***1.1 Problem Statement***

Measuring the constitutive parameters of materials at low frequencies using a rectangular waveguide-based apparatus demands that the sample under test (SUT) completely fill the waveguide's cross-sectional area if conventional methods such as the NWR (Nicholson-Wier-Ross) technique are to be used [1]-[4]. The NWR method assumes that the SUT is linear, homogeneous, isotropic, and that its surface planes are normal with respect to the incident wave's propagation vector. Because the SUT completely fills the waveguide's cross-section, there are no waveguide wall discontinuities. This implies that higher-order modes are not excited, leaving only the dominate  $TE_{10}$  (transverse electric) mode to propagate. However, low-frequency waveguides require large sample sizes, which can be very expensive and difficult to machine

The main focus of this work is to remove the requirement that the SUT completely fill the waveguide's cross-section and that the SUT only fill a two-dimensional waveguide reduction aperture. However, this reduced aperture sample holder disrupts the conventional waveguide wall surface currents and subsequently generates higher order ( $TE$ ) and transverse magnetic ( $TM$ ) modes. A rigorous modal analysis technique can be used to accommodate these higher-order  $TE$  and  $TM$  modes and will yield theoretical S-parameters that can be ported into a root searching and

optimization algorithm for iterative comparison with experimentally measured S-parameters leading to the SUT's frequency dependent constitutive parameters.

## ***1.2 Limitations***

Reducing the waveguide's cross-section by a near perfect electric conducting reduced aperture minimizes the transmitted power. This effect can potentially drive transmission coefficients down to the noise floor of the network analyzer and can be further complicated if the SUT is a high-loss material. The phenomenon will corrupt the constitutive parameter extraction process, which is critical to the proposed technique. The error analysis conducted within this effort will provide a better understanding of these limitations.

## ***1.3 Scope***

The work detailed in this thesis revolves around reducing an S-band waveguide cross-sectional area by 25%, 50%, and 75% with the reduced aperture having the same aspect ratio as the feeding waveguide. For example, the S-band waveguide used in this thesis has a width of 2.84 in. and height of 1.34 in. resulting in a cross-sectional area of 3.8056 in<sup>2</sup>. Reducing the waveguide's cross-sectional area by 25% implies that the reduced aperture will be 2.46 in. in width and 1.16 in. in height. These test configurations serve as a "proof-of-concept" that can later be applied to lower-frequency waveguide configurations. The materials characterized within this effort are self-supporting, meaning that they are not "sandwiched" between materials to maintain planar



rigidity. The analysis and programs developed by this effort are scalable and lend nicely to low-frequency material characterization via a user-friendly, graphical user interface driven program coded in Matlab<sup>®</sup>.

#### ***1.4 Thesis Organization***

Chapter 2 provides a theoretical background needed for later development and focuses on transverse electric and transverse magnetic modes in perfectly conducting rectangular waveguides and wave transmission matrices for analysis of multi-layer environments. Chapter 3 derives the modal-analysis technique that allows a smaller test sample to be mounted in a large waveguide and still determine the constitutive parameters of the material at the desired frequencies. Chapter 4 presents experimental results that verify the modal-analysis technique. In addition, a differential error analysis related to uncertainties in measuring test sample thickness and placement within the sample holder is conducted in Chapter 4 to form error bounds on the extracted material parameters. Finally, a set of conclusions and recommendations for future research are given in Chapter 5.

1. Introduction.....	1-1
1.1 Problem Statement.....	1-3
1.2 Limitations .....	1-4
1.3 Scope.....	1-4
1.4 Thesis Organization .....	1-5

## ***2. Background***

This chapter will derive the transverse electric ( $TE$ ) and transverse magnetic ( $TM$ ) fields that exist within a perfectly conducting rectangular waveguide and their respective modes. Next, the wave transmission matrices for both a single layer and multiple layers of material will be formulated and will be used in subsequent chapters.

### ***2.1 TE and TM Modes of a Rectangular Waveguide***

Because rectangular waveguides do not possess a center conductor, they cannot support transverse electromagnetic (TEM) waves [6], [7], but they can support both  $TE$  and/or  $TM$  waves. As will be shown, there are an infinite number of discrete solutions for both  $TE$  and  $TM$  waves that can potentially exist in rectangular waveguides. The  $TE_{10}$  field configuration is the dominate mode in a rectangular waveguide [6]-[9], and therefore was used as the excitation in all measurements associated with this thesis.

To identify the  $TE$  and  $TM$  mode solutions for the rectangular waveguide, it is mathematically convenient to separate the electric and magnetic field intensities ( $\vec{E}$  and  $\vec{H}$ ) into transverse and longitudinal components. The transverse components for this application lie in the x-y plane and the longitudinal components lie along the z-axis (see Figure 2.1).

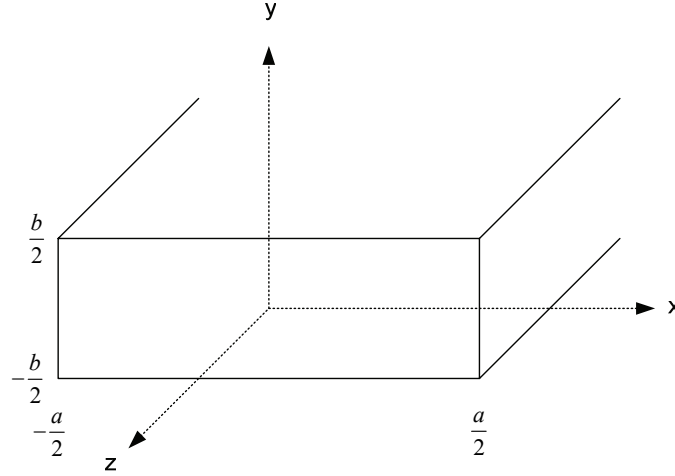


**Figure 2-1** Cross-sectional dimensions of the rectangular waveguide

For forward and reverse traveling waves, the electric and magnetic fields can be represented in the rectangular coordinate system as

$$\vec{E}(\vec{r}) = \vec{E}(\vec{\rho}, z) = \vec{E}_t(\vec{\rho}, z) \pm \hat{z} E_z(\vec{\rho}, z) = \vec{e}_t(\vec{\rho}) e^{\mp\gamma z} \pm \hat{z} e_z(\vec{\rho}) e^{\mp\gamma z} \quad (2.1)$$

$$\vec{H}(\vec{r}) = \vec{H}(\vec{\rho}, z) = \pm \vec{H}_t(\vec{\rho}, z) + \hat{z} H_z(\vec{\rho}, z) = \pm \vec{h}_t(\vec{\rho}) e^{\mp\gamma z} + \hat{z} h_z(\vec{\rho}) e^{\mp\gamma z} \quad (2.2)$$

where  $\vec{e}_t(\vec{\rho})$  and  $e_z(\vec{\rho})$  represent the transverse and longitudinal components of the

electric field respectively, and  $\vec{r} = \hat{x} x + \hat{y} y + \hat{z} z = \vec{\rho} + \hat{z} z$  with  $\vec{\rho} = \hat{x} x + \hat{y} y$ .

Similarly,  $\vec{h}_t(\vec{\rho})$  and  $h_z(\vec{\rho})$  represent the transverse and longitudinal components of the

magnetic field, respectively. Assuming an  $e^{j\omega t}$  time dependence, the negative exponential is associated with the forward-traveling wave and the positive exponential is associated with the reverse-traveling wave. The propagation constant  $\gamma$  is defined

through the well-known separation-of-variables constraint equation [7], namely

$$k^2 = \overbrace{k_x^2 + k_y^2}^{k_c^2} - \gamma^2 = k_c^2 - \gamma^2$$

$$\therefore \gamma = \sqrt{k_c^2 - k^2} \quad (2.3)$$

where

$$k = \omega \sqrt{\epsilon_{\text{complex}} \mu_{\text{complex}}}, \quad \epsilon_{\text{complex}} = \epsilon_{\text{real}} + j\epsilon_{\text{imaginary}}, \quad \text{and} \quad \mu_{\text{complex}} = \mu_{\text{real}} + j\mu_{\text{imaginary}}$$

**Note:**

The “complex” subscript will be suppressed throughout the remainder of this manuscript for notational convenience.

**2.1.1 Maxwell’s Equations**

The basic forms of Maxwell’s equations for a linear, homogeneous, isotropic material are (with  $e^{j\omega t}$  assumed and suppressed)

$$\nabla \times \vec{E} = -\vec{M}_i - j\omega\mu\vec{H} \quad (2.4)$$

$$\nabla \times \vec{H} = \vec{J}_i + \vec{J}_c + j\omega\epsilon\vec{E} \quad (2.5)$$

$$\nabla \cdot \vec{E} = \frac{q_{ev}}{\epsilon} \quad (2.6)$$

$$\nabla \cdot \vec{H} = \frac{q_{mv}}{\mu} \quad (2.7)$$

where

$\vec{E}$  = electric field intensity (volts/meter)

$\vec{M}_i$  = impressed (source) magnetic current density (volts/square meter)

$\vec{H}$  = magnetic field intensity (amperes/meter)

$\vec{J}_i$  = impressed (source) electric current density (amperes/square meter)

$\vec{J}_c$  = conduction electric current density (amperes/square meter)

$q_{ev}$  = electric charge density (coulombs/cubic meter)

$q_{mv}$  = magnetic charge density (webers/cubic meters)

In a source-free region of the waveguide, Maxwell's equations reduce to

$$\nabla \times \vec{E} = -j\omega\mu\vec{H} \quad (2.8)$$

$$\nabla \times \vec{H} = j\omega\varepsilon\vec{E} \quad (2.9)$$

$$\nabla \cdot \vec{E} = 0 \quad (2.10)$$

$$\nabla \cdot \vec{H} = 0 \quad (2.11)$$

Now that Maxwell's equations have been properly configured for the sample holder region inside the rectangular waveguide,  $\vec{E}$  and  $\vec{H}$  can be replaced by their transverse and longitudinal representations as derived in (2.1) and (2.2), respectively. If the "del" operator is decomposed into its transverse and longitudinal components as follows

$$\begin{aligned} \nabla &= \nabla_t + \hat{z} \frac{\partial}{\partial z} \\ \Rightarrow \nabla_t &= \hat{x} \frac{\partial}{\partial x} + \hat{y} \frac{\partial}{\partial y} \end{aligned} \quad (2.12)$$

then, Maxwell's equations simplify to the following expressions

$$\nabla_t \times \vec{e}_t(\vec{\rho}) = -\hat{z} j\omega\mu h_z(\vec{\rho}) \quad \dots \text{for } TE \text{ modes} \quad (2.13a)$$

$$\nabla_t \times \vec{e}_t(\vec{\rho}) = 0 \quad \dots \text{for } TM \text{ modes} \quad (2.13b)$$

$$\gamma \hat{z} \times \vec{e}_t(\vec{\rho}) = j\omega\mu \vec{h}_t(\vec{\rho}) \quad \dots \text{for } TE \text{ modes} \quad (2.14a)$$

$$\hat{z} \times \nabla_t e_z(\vec{\rho}) + \gamma \hat{z} \times \vec{e}_t(\vec{\rho}) = j\omega\mu \vec{h}_t(\vec{\rho}) \quad \text{for } TM \text{ modes} \quad (2.14b)$$

$$\nabla_t \times \vec{h}_t(\vec{\rho}) = 0 \quad \text{for } TE \text{ modes} \quad (2.15a)$$

$$\nabla_t \times \vec{h}_t(\vec{\rho}) = j\omega\epsilon e_z(\vec{\rho}) \quad \text{for } TM \text{ modes} \quad (2.15b)$$

$$\hat{z} \times \nabla_t h_z(\vec{\rho}) + \gamma \hat{z} \times \vec{h}_t(\vec{\rho}) = -j\omega\epsilon \vec{e}_t(\vec{\rho}) \quad \text{for } TE \text{ modes} \quad (2.16a)$$

$$\gamma \hat{z} \times \vec{h}_t(\vec{\rho}) = -j\omega\epsilon \vec{e}_t(\vec{\rho}) \quad \text{for } TM \text{ modes} \quad (2.16b)$$

$$\nabla_t \cdot \vec{e}_t(\vec{\rho}) = 0 \quad \text{for } TE \text{ modes} \quad (2.17a)$$

$$\nabla_t \cdot \vec{e}_t(\vec{\rho}) = \gamma e_z(\vec{\rho}) \quad \text{for } TM \text{ modes} \quad (2.17b)$$

$$\nabla_t \cdot \vec{h}_t(\vec{\rho}) = \gamma h_z(\vec{\rho}) \quad \text{for } TE \text{ modes} \quad (2.18a)$$

$$\nabla_t \cdot \vec{h}_t(\vec{\rho}) = 0 \quad \text{for } TM \text{ modes} \quad (2.18b)$$

### 2.1.2 Helmholtz Wave Equation

By inspecting (2.13) thru (2.16), it is evident that the electric and magnetic fields are coupled. For our application, it is necessary to uncouple the fields and relate the transverse and longitudinal components. The penalty for uncoupling the two fields is that the order of differentiation will be increased by one, resulting in the familiar Helmholtz

wave equation. To accomplish this task, we start by taking the curl of both sides of (2.8), which yields

$$\nabla \times \nabla \times \vec{E} = \nabla \times -j\omega\mu\vec{H} = -j\omega\mu(\nabla \times \vec{H})$$

Using the vector identity  $\nabla \times \nabla \times \vec{E} = \nabla(\nabla \cdot \vec{E}) - \nabla^2 \vec{E}$  and substituting (2.9) for the curl of magnetic field intensity ( $\nabla \times \vec{H}$ ) provides

$$\nabla(\nabla \cdot \vec{E}) - \nabla^2 \vec{E} = -j\omega\mu(j\omega\varepsilon\vec{E}) = \omega^2\mu\varepsilon\vec{E} = k^2\vec{E}$$

Now, substituting (2.10) for the divergence of the electric field intensity ( $\nabla \cdot \vec{E}$ ), letting  $k^2 = \omega^2\mu\varepsilon$  ( $k$  is the complex wave number), and transposing either term gives the Helmholtz wave equation for an electric field

$$\nabla^2 \vec{E} + k^2 \vec{E} = 0 \quad (2.19)$$

The procedure used in this section can also be applied to (2.9) to produce

$$\nabla^2 \vec{H} + k^2 \vec{H} = 0 \quad (2.20)$$

### 2.1.3 Helmholtz Wave Equation Applied to Rectangular Waveguide

To identify the *TE* and *TM* mode solutions for the rectangular waveguide, the Helmholtz equations are separated into transverse and longitudinal components, as follows

$$\nabla_t^2 \vec{e}_t(\vec{\rho}) + k_c^2 \vec{e}_t(\vec{\rho}) = 0 \quad (2.21)$$

$$\nabla_t^2 e_z(\vec{\rho}) + k_c^2 e_z(\vec{\rho}) = 0 \quad (2.22)$$



$$\nabla_t^2 \vec{h}_t(\vec{\rho}) + k_c^2 \vec{h}_t(\vec{\rho}) = 0 \quad (2.23)$$

$$\nabla_t^2 h_z(\vec{\rho}) + k_c^2 h_z(\vec{\rho}) = 0 \quad (2.24)$$

$$\text{where: } k_c^2 = \gamma^2 + k^2$$

For the *TE* case where  $e_z(\vec{\rho}) = 0$ ,  $\vec{h}_t(\vec{\rho})$  can be found in terms of  $h_z(\vec{\rho})$  by taking the transverse curl of (2.15a), applying the vector identity (a.k.a. “back cab” rule)  $\vec{A} \times (\vec{B} \times \vec{C}) = \vec{B}(\vec{A} \cdot \vec{C}) - \vec{C}(\vec{A} \cdot \vec{B})$ , substituting  $\nabla_t \cdot \vec{h}_t(\vec{\rho}) = \gamma h_z(\vec{\rho})$ , then substituting  $\nabla_t^2 \vec{h}_t(\vec{\rho}) = -k_c^2 \vec{h}_t(\vec{\rho})$  from (2.23). Solving for  $\vec{h}_t(\vec{\rho})$  using simple algebra provides the following result

$$\vec{h}_t(\vec{\rho}) = -\frac{\gamma}{k_c^2} \nabla_t h_z(\vec{\rho}) \quad (2.25)$$

Now, that  $\vec{h}_t(\vec{\rho})$  is in terms of  $h_z(\vec{\rho})$ , we can apply a similar procedure and solve for  $\vec{e}_t(\vec{\rho})$  in terms of  $\vec{h}_t(\vec{\rho})$ . To do this, (2.14a) is cross-multiplied by  $\hat{z}$  and the “back cab” rule applied. Realizing that  $\hat{z} \cdot \vec{e}_t(\vec{\rho}) = 0$  and  $\hat{z} \cdot \hat{z} = 1$  provides

$$\vec{e}_t(\vec{\rho}) = -Z_{TE} \hat{z} \times \vec{h}_t(\vec{\rho}) \quad (2.26)$$

$$\text{where } Z_{TE} = \frac{j\omega\mu}{\gamma}$$

It is important to note that if  $h_z(\vec{\rho})$  is known for the *TE* case,  $\vec{h}_t(\vec{\rho})$  and  $\vec{e}_t(\vec{\rho})$  can be calculated using (2.25) and (2.26). This produces all of the *TE*-based fields existing in the waveguide for any given *TE* mode.

For the *TM* case where  $h_z(\vec{\rho})=0$ ,  $\vec{e}_t(\vec{\rho})$  can be found in terms of  $e_z(\vec{\rho})$  by taking the transverse curl of (2.13b), applying “back cab”, substituting  $\nabla_t \bullet \vec{e}_t(\vec{\rho}) = \gamma e_z(\vec{\rho})$ , then substituting  $\nabla_t^2 \vec{e}_t(\vec{\rho}) = -k_c^2 \vec{e}_t(\vec{\rho})$  from (2.21). Finally, solving for  $\vec{e}_t(\vec{\rho})$  provides the following

$$\vec{e}_t(\vec{\rho}) = -\frac{\gamma}{k_c^2} \nabla_t e_z(\vec{\rho}) \quad (2.27)$$

Similar to the *TE* case, (2.16b) is cross-multiplied by  $\hat{z}$  and the “back cab” rule applied.

Substituting  $\hat{z} \bullet \vec{h}_t(\vec{\rho}) = 0$  and  $\hat{z} \bullet \hat{z} = 1$  yields

$$\vec{h}_t(\vec{\rho}) = \frac{\hat{z} \times \vec{e}_t(\vec{\rho})}{Z_{TM}} \quad (2.28)$$

$$\text{where } Z_{TM} = \frac{\gamma}{j\omega\epsilon}$$

In summary, if  $e_z(\vec{\rho})$  is known for the *TM* case, both  $\vec{e}_t(\vec{\rho})$  and  $\vec{h}_t(\vec{\rho})$  can be calculated using (2.27) and (2.28). This produces all of the *TM*-based fields existing in a rectangular waveguide for any given *TM* mode.

#### 2.1.4 Separation of Variables

Based on prior knowledge of  $h_z(\vec{\rho})$  and  $e_z(\vec{\rho})$ , all field components of both the *TE* and *TM* modes can be developed using (2.25) thru (2.28). Producing the initial expressions for  $h_z(\vec{\rho})$  and  $e_z(\vec{\rho})$  is accomplished by solving the scalar wave equations

for  $h_z(\vec{\rho})$  and  $\vec{e}_z(\vec{\rho})$ , (2.19) and (2.20) respectively, using the separation of variables method.

For the *TE* case,  $h_z(\vec{\rho})$  must be found before the remaining field components can be calculated using (2.25) and (2.26). Therefore, assuming

$h_z(\vec{\rho}, z) = h_z(x, y, z) = X(x)Y(y)Z(z)$  and recognizing  $\nabla = \frac{\partial^2}{\partial x^2} + \frac{\partial^2}{\partial y^2} + \frac{\partial^2}{\partial z^2}$  reduces (2.19) to

$$\left( \frac{\partial^2}{\partial x^2} + \frac{\partial^2}{\partial y^2} + \frac{\partial^2}{\partial z^2} \right) X(x)Y(y)Z(z) + X(x)Y(y)Z(z)k^2 = 0$$

After some simple algebra and dividing through by  $X(x)Y(y)Z(z)$  yields

$$\underbrace{\frac{1}{X(x)} \frac{\partial^2}{\partial x^2} X(x)}_{=-k_x^2} + \underbrace{\frac{1}{Y(y)} \frac{\partial^2}{\partial y^2} Y(y)}_{=-k_y^2} + \underbrace{\frac{1}{Z(z)} \frac{\partial^2}{\partial z^2} Z(z)}_{=-k_z^2} + k^2 = 0 \quad (2.29)$$

Realizing  $\frac{1}{X(x)} \frac{\partial^2}{\partial x^2} X(x)$ ,  $\frac{1}{Y(y)} \frac{\partial^2}{\partial y^2} Y(y)$  and  $\frac{1}{Z(z)} \frac{\partial^2}{\partial z^2} Z(z)$  are equal to constants labeled as  $-k_x^2$ ,  $-k_y^2$  and  $-k_z^2$  respectively, makes  $k^2 = k_x^2 + k_y^2 + k_z^2$ . Performing basic

algebra on (2.29) results in three separate ordinary differential equations as follows

$$\frac{d^2 X(x)}{dx^2} + k_x^2 X(x) = 0 \quad (2.30)$$

$$\frac{d^2 Y(y)}{dy^2} + k_y^2 Y(y) = 0 \quad (2.31)$$

$$\frac{d^2 Z(z)}{dz^2} + k_z^2 Z(z) = 0 \quad (2.32)$$

The solutions to (2.30) thru (2.32) are as follows

$$X(x) = \begin{cases} A_1 \cos k_x x + B_1 \sin k_x x & \dots \text{for standing waves} \\ \text{-or-} \\ A_1 e^{-jk_x x} + B_1 e^{jk_x x} & \dots \text{for traveling waves} \end{cases} \quad (2.33)$$

$$Y(y) = \begin{cases} A_2 \cos k_y y + B_2 \sin k_y y & \dots \text{for standing waves} \\ \text{-or-} \\ A_2 e^{-jk_y y} + B_2 e^{jk_y y} & \dots \text{for traveling waves} \end{cases} \quad (2.34)$$

$$Z(z) = \begin{cases} A_3 \cos k_z z + B_3 \sin k_z z & \dots \text{for standing waves} \\ \text{-or-} \\ A_3 e^{-jk_z z} + B_3 e^{jk_z z} & \dots \text{for traveling waves} \end{cases} \quad (2.35)$$

where  $\gamma = jk_z$  was derived in (2.3)

The rectangular waveguide is bounded in both the  $x$  and  $y$  directions, but unbounded in the  $z$  direction. This results in standing waves for both  $x$  and  $y$  axes and traveling waves for the  $z$ -axis. Therefore, the appropriate solution to  $h_z(\vec{\rho}, z)$  is

$$h_z(\vec{\rho}, z) = h_z(x, y, z) = X(x)Y(y)Z(z) = (A_1 \cos k_x x + B_1 \sin k_x x) \cdot (A_2 \cos k_y y + B_2 \sin k_y y) \cdot (A_3^+ e^{-\gamma z} + A_3^- e^{\gamma z}) \quad (2.36)$$

where  $A_3^+$  and  $A_3^-$  represent the complex wave amplitudes in the positive and negative  $z$ -direction, respectively. Accordingly, the negative exponential denotes a positive traveling wave and the positive exponential denotes a negative traveling wave. Equation (2.36) suggests that the origin of the coordinate system is located at the bottom left corner

of the waveguide (see Fig 2.1). To facilitate analysis, the origin is shifted to the center of the rectangular waveguide. This means the solution to  $h_z(\bar{\rho}, z)$  has to be modified such that

$$h_z(\bar{\rho}, z) = \left[ A_1 \cos k_x \left( x + \frac{a}{2} \right) + B_1 \sin k_x \left( x + \frac{a}{2} \right) \right] \cdot \left[ A_2 \cos k_y \left( y + \frac{b}{2} \right) + B_2 \sin k_y \left( y + \frac{b}{2} \right) \right] \cdot (A_3^+ e^{-\gamma z} + A_3^- e^{\gamma z}) \quad (2.37)$$

The process just described allowed the derivation of  $h_z(\bar{\rho}, z)$  using separation of variables and selection of the appropriate solution for the ordinary differential equations encountered. The same procedure can be accomplished for the *TM* case where

$h_z(\bar{\rho}, z) = 0$  and a solution to  $e_z(\bar{\rho}, z) = e_z(x, y, z)$  is

$$e_z(\bar{\rho}, z) = \left[ A_1 \cos k_x \left( x + \frac{a}{2} \right) + B_1 \sin k_x \left( x + \frac{a}{2} \right) \right] \cdot \left[ A_2 \cos k_y \left( y + \frac{b}{2} \right) + B_2 \sin k_y \left( y + \frac{b}{2} \right) \right] \cdot (A_3^+ e^{-\gamma z} + A_3^- e^{\gamma z}) \quad (2.38)$$

### 2.1.5 Application of Waveguide's Boundary Conditions

For rectangular waveguides, each wall is typically considered to be a perfect electric conductor, which means the tangential electric field at each wall is equal to zero.

This condition expressed in mathematical terms is

$$\hat{n} \times \vec{E} \Big|_{walls} = 0 \quad (2.39)$$

Starting with the *TE* case where  $e_z(\vec{\rho}) = e_z(x, y) = 0$ , (2.37) is reduced to

$$\hat{n} \times \vec{e}_t(\vec{\rho}) \Big|_{\text{walls}} = 0 \quad (2.40)$$

If  $\vec{e}_t(\vec{\rho})$  is replaced by (2.26), “back cab” rule is applied, and  $\vec{h}_t(\vec{\rho})$  replaced by (2.25),

a little algebra will provide

$$\hat{n} \bullet \nabla_t h_z(\vec{\rho}) \Big|_{\text{walls}} = 0 \quad (2.41)$$

By inspecting Figure 2.1, it is apparent that  $\hat{n} = \hat{x}$  for the left vertical wall,  $\hat{n} = -\hat{x}$  for the right vertical wall,  $\hat{n} = \hat{y}$  for the bottom wall, and  $\hat{n} = -\hat{y}$  for the top wall. Each wall has to be addressed and the appropriate boundary condition (2.41) applied. Therefore, starting with the left vertical wall and using (2.37),

$$\hat{x} \bullet \nabla_t h_z(\vec{\rho}, z) \Big|_{\substack{x=-\frac{a}{2} \\ \frac{b}{2} \leq y \leq \frac{b}{2} \\ -\infty \leq z \leq \infty}} = 0 \quad \Rightarrow B_1 = 0 \quad (2.42)$$

For right vertical wall

$$-\hat{x} \bullet \nabla_t h_z(\vec{\rho}, z) \Big|_{\substack{x=\frac{a}{2} \\ \frac{b}{2} \leq y \leq \frac{b}{2} \\ -\infty \leq z \leq \infty}} = 0 \quad \Rightarrow k_{x,m} = \frac{m\pi}{a} \quad \text{where } m = 0, 1, 2, 3, \dots \quad (2.43)$$

For bottom wall

$$\hat{y} \bullet \nabla_t h_z(\vec{\rho}, z) \Big|_{\substack{y=-\frac{b}{2} \\ \frac{a}{2} \leq x \leq \frac{a}{2} \\ -\infty \leq z \leq \infty}} = 0 \quad \Rightarrow B_2 = 0 \quad (2.44)$$

Finally, the top wall

$$-\hat{y} \bullet \nabla_t h_z(\vec{\rho}, z) \Big|_{\substack{y=\frac{b}{2} \\ \frac{a}{2} \leq x \leq \frac{a}{2} \\ -\infty \leq z \leq \infty}} = 0 \quad \Rightarrow k_{y,n} = \frac{n\pi}{b} \quad \text{where } n = 0, 1, 2, 3, \dots \quad (2.45)$$

Incorporating the results from (2.40)-(2.43) into  $\vec{h}_z(\vec{\rho})$  produces

$$h_z(\vec{\rho}, z) = \cos k_{x,m} \left( x + \frac{a}{2} \right) \cos k_{y,n} \left( y + \frac{b}{2} \right) (A_3^+ e^{-\gamma z} + A_3^- e^{\gamma z}) \quad (2.46)$$

where  $A_1 A_2$  were combined into the complex amplitudes  $A_3^+$  and  $A_3^-$

Now that  $h_z(\vec{\rho}, z)$  has been refined to satisfy the waveguide's boundary

conditions, the remaining components of the magnetic field intensity are easily found using (2.25) and all of the electric field components can be found via (2.26). A summary of the fields for the *TE* mode are provided by (2.47) thru (2.52).

$$h_{x,mn}(\vec{\rho}, z) = \frac{\gamma_{mn} k_{x,n}}{k_{c,mn}^2} \sin k_{x,m} \left( x + \frac{a}{2} \right) \cos k_{y,n} \left( y + \frac{b}{2} \right) (A_3^+ e^{-\gamma z} + A_3^- e^{\gamma z}) \quad (2.47)$$

$$h_{y,mn}(\vec{\rho}, z) = \frac{\gamma_{mn} k_{y,n}}{k_{c,mn}^2} \cos k_{x,m} \left( x + \frac{a}{2} \right) \sin k_{y,n} \left( y + \frac{b}{2} \right) (A_3^+ e^{-\gamma z} + A_3^- e^{\gamma z}) \quad (2.48)$$

$$h_{z,mn}(\vec{\rho}, z) = \cos k_{x,m} \left( x + \frac{a}{2} \right) \cos k_{y,n} \left( y + \frac{b}{2} \right) (A_3^+ e^{-\gamma z} + A_3^- e^{\gamma z}) \quad (2.49)$$

$$e_{x,mn}(\vec{\rho}, z) = \frac{j\omega\mu k_{y,n}}{k_{c,mn}^2} \cos k_{x,m} \left( x + \frac{a}{2} \right) \sin k_{y,n} \left( y + \frac{b}{2} \right) (A_3^+ e^{-\gamma z} + A_3^- e^{\gamma z}) \quad (2.50)$$

$$e_{y,mn}(\vec{\rho}, z) = -\frac{j\omega\mu k_{x,m}}{k_{c,mn}^2} \sin k_{x,m} \left( x + \frac{a}{2} \right) \cos k_{y,n} \left( y + \frac{b}{2} \right) (A_3^+ e^{-\gamma z} + A_3^- e^{\gamma z}) \quad (2.51)$$

$$e_z(\vec{\rho}, z) = 0 \quad (2.52)$$

It is important to note that if both  $m$  and  $n$  are equal to zero, all of the field components reduce to zero, providing a trivial solution. This restriction aside, the number of possible  $m$  and  $n$  combinations (*TE* modes) are unbounded, hence the infinite number of solutions mentioned at the beginning of this section. The good news is that

there is an order to the modes that is solely dependent on the waveguide's geometry, and is derived in section 2.1.6.

For the *TM* case where  $h_z(\vec{\rho}, z) = 0$ , (2.38) provides the expression for  $e_z(\vec{\rho}, z)$ .

The *x*-component and *y*-component of the electric field,  $e_x(\vec{\rho}, z)$  and  $e_y(\vec{\rho}, z)$

respectively, can be found through application of (2.27) resulting in

$$e_x(\vec{\rho}, z) = e_x(x, y) = \frac{\gamma k_x}{k_c^2} \left[ C_1 \sin k_x \left( x + \frac{a}{2} \right) - D_1 \cos k_x \left( x + \frac{a}{2} \right) \right] \cdot \left[ C_2 \cos k_y \left( y + \frac{b}{2} \right) + D_2 \sin k_y \left( y + \frac{b}{2} \right) \right] \cdot (A_3^+ e^{-\gamma z} + A_3^- e^{\gamma z}) \quad (2.53)$$

$$e_y(\vec{\rho}, z) = e_y(x, y) = \frac{\gamma k_y}{k_c^2} \left[ C_1 \cos k_x \left( x + \frac{a}{2} \right) + D_1 \sin k_x \left( x + \frac{a}{2} \right) \right] \cdot \left[ C_2 \sin k_y \left( y + \frac{b}{2} \right) - D_2 \cos k_y \left( y + \frac{b}{2} \right) \right] \cdot (A_3^+ e^{-\gamma z} + A_3^- e^{\gamma z}) \quad (2.54)$$

Keep in mind that (2.38), (2.53), and (2.54) do not consider the boundary conditions at the waveguide's walls. Therefore, the tangential electric field boundary condition expressed in (2.39) must be imposed directly to the applicable electric field components. Starting with the left vertical wall and observing Figure 2-1, we know that the tangential electric field components are  $e_y(\vec{\rho}, z)$  and  $e_z(\vec{\rho}, z)$ . Imposing (2.39) on the left vertical wall yields

$$e_y(\vec{\rho}, z) \Big|_{\substack{x=-\frac{a}{2} \\ \frac{b}{2} \leq y \leq \frac{b}{2} \\ -\infty \leq z \leq \infty}} = 0 \quad \text{and} \quad e_z(\vec{\rho}, z) \Big|_{\substack{x=-\frac{a}{2} \\ \frac{b}{2} \leq y \leq \frac{b}{2} \\ -\infty \leq z \leq \infty}} = 0 \quad \Rightarrow C_1 = 0 \quad (2.55)$$



For the right vertical wall,  $e_y(\vec{\rho}, z)$  and  $e_z(\vec{\rho}, z)$  are again the tangential electric field components. As such,

$$e_y(\vec{\rho}, z)\Big|_{\substack{x=\frac{a}{2} \\ \frac{b}{2} \leq y \leq \frac{b}{2} \\ -\infty \leq z \leq \infty}} = 0 \quad \text{and} \quad e_z(\vec{\rho}, z)\Big|_{\substack{x=\frac{a}{2} \\ \frac{b}{2} \leq y \leq \frac{b}{2} \\ -\infty \leq z \leq \infty}} = 0 \quad \Rightarrow k_{x,r} = \frac{r\pi}{a} \quad \text{where } r = 1, 2, 3 \dots \quad (2.56)$$

For the bottom wall,  $e_x(\vec{\rho}, z)$  and  $e_z(\vec{\rho}, z)$  are the tangential electric field components.

As such,

$$e_x(\vec{\rho}, z)\Big|_{\substack{y=\frac{b}{2} \\ \frac{a}{2} \leq x \leq \frac{a}{2} \\ -\infty \leq z \leq \infty}} = 0 \quad \text{and} \quad e_z(\vec{\rho}, z)\Big|_{\substack{y=\frac{b}{2} \\ \frac{a}{2} \leq x \leq \frac{a}{2} \\ -\infty \leq z \leq \infty}} = 0 \quad \Rightarrow C_2 = 0 \quad (2.57)$$

Lastly, for the top wall where  $e_x(\vec{\rho}, z)$  and  $e_z(\vec{\rho}, z)$  are again the tangential electric field components

$$e_x(\vec{\rho}, z)\Big|_{\substack{y=\frac{b}{2} \\ \frac{a}{2} \leq x \leq \frac{a}{2} \\ -\infty \leq z \leq \infty}} = 0 \quad \text{and} \quad e_z(\vec{\rho}, z)\Big|_{\substack{y=\frac{b}{2} \\ \frac{a}{2} \leq x \leq \frac{a}{2} \\ -\infty \leq z \leq \infty}} = 0 \quad \Rightarrow k_{y,s} = \frac{s\pi}{b} \quad \text{where } s = 1, 2, 3 \dots \quad (2.58)$$

Incorporating the results from (2.55)-(2.58) into (2.38), (2.54), and (2.55) yields the electric field components. The magnetic field components can be found by applying (2.28). All *TM* field components are summarized in (2.57)-(2.62).

$$e_{x,rs}(\vec{\rho}, z) = -\frac{\gamma_{rs} k_{x,r}}{k_{c,rs}^2} \cos k_{x,r} \left( x + \frac{a}{2} \right) \sin k_{y,s} \left( y + \frac{b}{2} \right) (B_3^+ e^{-\gamma z} + B_3^- e^{\gamma z}) \quad (2.59)$$

$$e_{y,rs}(\vec{\rho}, z) = -\frac{\gamma_{rs} k_{y,r}}{k_{c,rs}^2} \sin k_{x,r} \left( x + \frac{a}{2} \right) \cos k_{y,s} \left( y + \frac{b}{2} \right) (B_3^+ e^{-\gamma z} + B_3^- e^{\gamma z}) \quad (2.60)$$

$$e_{z,rs}(\vec{\rho}, z) = \sin k_{x,r} \left( x + \frac{a}{2} \right) \sin k_{y,s} \left( y + \frac{b}{2} \right) (B_3^+ e^{-\gamma z} + B_3^- e^{\gamma z}) \quad (2.61)$$

$$h_{x,rs}(\vec{\rho}, z) = \frac{j\omega\varepsilon k_{y,s}}{k_{c,rs}^2} \sin k_{x,r} \left( x + \frac{a}{2} \right) \cos k_{y,s} \left( y + \frac{b}{2} \right) (B_3^+ e^{-\gamma z} + B_3^- e^{\gamma z}) \quad (2.62)$$

$$h_{y,rs}(\vec{\rho}, z) = -\frac{j\omega\varepsilon k_{x,r}}{k_{c,rs}^2} \cos k_{x,r} \left( x + \frac{a}{2} \right) \sin k_{y,s} \left( y + \frac{b}{2} \right) (B_3^+ e^{-\gamma z} + B_3^- e^{\gamma z}) \quad (2.63)$$

$$h_{z,rs}(\vec{\rho}, z) = 0 \quad (2.64)$$

where  $D_1 D_2$  were combined into the complex amplitude coefficients  $B_3^+$  and  $B_3^-$ .

It is important to note that the only restriction on the *TM* mode indices ( $r$  and  $s$ ) is that  $s$  never equal to zero as indicated in (2.58). By inspecting (2.59) – (2.64), it is evident that if  $s$  equals zero, all of the field components reduce to zero, leading to the trivial solution. Like the *TE* case, there are an infinite number of discrete modes for the *TM* fields and the order of these modes is also solely dependent on the waveguide's geometry and is described in Section 2.1.6. Finally, the field components derived in this section can be used to account for reflections at waveguide wall discontinuities. The reduced aperture will introduce a waveguide wall disruption, and will be analyzed in Chapter 3.

### 2.1.6 Order of Modes Determined by Cut-off Frequency

As mentioned earlier, there are an infinite number of modes for both the *TE* and *TM* field configurations. The order of the modes is determined by the waveguide's aspect ratio and can be found by determining the various cut-off frequencies, which are defined as the frequencies separating the propagation and no-propagation bands [6]. For the waveguide defined in this document, waves propagate in the  $\pm z$ -direction. Therefore,

cut-off occurs when the wave ceases to propagate in the  $\pm z$ -direction, implying that the respective propagation constant ( $\gamma$ ) is zero. From (2.3), we know that

$$k_c^2 = \gamma^2 + k^2 \quad (2.65)$$

$$\text{where, } k_c^2 = k_x^2 + k_y^2$$

By letting the propagation constant ( $\gamma$ ) go to zero,  $k_c^2 = k^2$  results where  $k^2 = \omega_c^2 \mu \epsilon$  and  $\omega_c = 2\pi f_c$ . After some basic algebra, the following relationships are found

$$f_c = \begin{cases} \frac{c}{2\pi\sqrt{\epsilon_r\mu_r}} \sqrt{\left(\frac{m\pi}{a}\right)^2 + \left(\frac{n\pi}{b}\right)^2} & \dots\text{for TE-modes} \\ \frac{c}{2\pi\sqrt{\epsilon_r\mu_r}} \sqrt{\left(\frac{r\pi}{a}\right)^2 + \left(\frac{s\pi}{b}\right)^2} & \dots\text{for TM-modes} \end{cases} \quad (2.66)$$

For either field configuration (*TE* or *TM*), all of the terms are constant with the exception of the indices  $m$  and  $n$  for the *TE*-mode, and  $r$  and  $s$  for the *TM*-mode. Therefore, the order of the modes is dictated by the different combinations of these indices with each combination producing a set cut-off frequency. The indices that produce the lowest cut-off frequency is the first mode, the indices that produce the next higher cut-off frequency is the second mode and so forth. For the S-band waveguide used in this thesis where  $a = 2.84$  inches and  $b = 1.34$  inches, the first *TE* mode occurs when  $m = 1$  and  $n = 0$  producing a cut-off frequency of  $\sim 2.1$  GHz for the respective  $TE_{10}$  mode. The next higher-order mode occurs when  $m = 2$  and  $n = 0$  producing a cut-off frequency of 4.2 GHz for the respective  $TE_{20}$  mode. For the same waveguide, the first *TM* mode occurs when  $r = 1$  and  $s = 1$  producing a cut-off frequency of 4.9 GHz for the  $TM_{11}$  mode. The next higher *TM* mode for the S-band waveguide is the  $TM_{21}$  field

configuration with a cut-off frequency of 6.1 GHz. Therefore, if the S-band waveguide was operated at frequencies greater than 2.1 GHz, but less than 4.2 GHz, only the  $TE_{10}$  mode would propagate within the waveguide, making it the dominate mode.

## 2.2 Wave Transmission Matrices (A-Parameters)

A-parameters are the elements of a  $2 \times 2$  matrix that establish the relationship between incident, reflected, and transmitted complex wave amplitudes at defined measurement planes. The A-parameters are derived from analyzing reflection and transmission at multiple interfaces for both lossless and lossy mediums. For this thesis, only the test sample was placed inside the sample holder with the sample completely filling the sample holder, flush on both sides. Regardless of the single-layer configuration used in this thesis, portions of the MatLab<sup>®</sup> code used to implement the solution were incorporated from a previous effort [10]. As such, the Matlab program can accommodate single or multiple layer configurations. In an attempt to thoroughly address each case, this section will start by defining the A-parameters for a single layer medium, A-parameters for multiple layers, then modifying each case to match the sample holder's configurations.

### 2.2.1 A-parameters for Single Layer Configuration

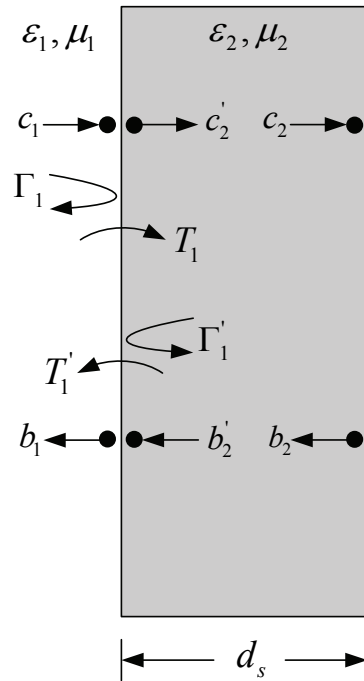


**Figure 2-2** Layout of single layer material with reflected waves and transmitted waves

Before multi-layer sample holder configurations can be addressed, the basic single layer case must be fully comprehended as more complex cases are built from the basic single layer interface A-parameters. By inspecting figure 2.2, it is apparent that the following relations hold

$$b_1 = \Gamma_1 c_1 + T_1' b_2' \quad (2.67)$$

$$c_2' = T_1 c_1 + \Gamma_1' b_2' \quad (2.68)$$

Solving (2.68) for  $c_1$  leads to

$$c_1 = \left(\frac{1}{T_1}\right)c_2' - \left(\frac{\Gamma_1'}{T_1}\right)b_2' \quad (2.69)$$

Substituting (2.69) into (2.67) and a little algebraic manipulation provides

$$b_1 = \left(\frac{\Gamma_1}{T_1}\right)c_2' + \left(\frac{T_1'T_1 - \Gamma_1'}{T_1}\right)b_2' \quad (2.70)$$

In matrix form, (2.69) and (2.70) become

$$\begin{bmatrix} c_1 \\ b_1 \end{bmatrix} = \frac{1}{T_1} \begin{bmatrix} 1 & -\Gamma_1' \\ \Gamma_1 & T_1'T_1 - \Gamma_1' \end{bmatrix} \begin{bmatrix} c_2' \\ b_2' \end{bmatrix} \quad (2.71)$$

The reflection and transmission coefficients ( $\Gamma_1, \Gamma_1', T_1,$  and  $T_1'$ ) are determined by enforcing continuity of the tangential components of the electric and magnetic fields across the planar interface. Enforcement of these conditions results in the following well-known relations

$$T_1 = 1 + \Gamma_1 \quad (2.72)$$

$$\Gamma_1' = -\Gamma_1 \quad (2.73)$$

$$T_1' = 1 + \Gamma_1' = 1 - \Gamma_1 \quad (2.74)$$

Substituting (2.72) thru (2.74) into (2.71) reduces (2.71) to

$$\begin{bmatrix} c_1 \\ b_1 \end{bmatrix} = \frac{1}{T_1} \begin{bmatrix} 1 & \Gamma_1 \\ \Gamma_1 & 1 \end{bmatrix} \begin{bmatrix} c_2' \\ b_2' \end{bmatrix} \quad (2.75)$$

$$\text{where: } \Gamma_1 = \frac{Z_2 - Z_1}{Z_2 + Z_1}$$

and  $Z_1$  and  $Z_2$  are the wave impedances in medium 1 and 2 respectively. Equation (2.75) relates the complex wave amplitudes for the forward and reverse traveling waves at  $c_1$  and  $b_1$  to the complex wave amplitudes for the forward and reverse traveling waves at  $c_2'$  and  $b_2'$ . To derive the complex wave amplitudes for the forward and reverse propagating waves at  $c_2$  and  $b_2$ , the complex wave amplitudes at  $c_2'$  and  $b_2'$  must be translated to the right a distance of  $d_s$  via a propagation phase delay. Assuming that medium 2 is linear, homogeneous, and isotropic, the following relationships hold

$$c_2' = c_2 e^{\gamma_2 d_s} \quad (2.76)$$

$$b_2' = b_2 e^{-\gamma_2 d_s} \quad (2.77)$$

In matrix form, (2.76) and (2.77) become

$$\begin{bmatrix} c_2' \\ b_2' \end{bmatrix} = \begin{bmatrix} e^{\gamma_2 d_s} & 0 \\ 0 & e^{-\gamma_2 d_s} \end{bmatrix} \begin{bmatrix} c_2 \\ b_2 \end{bmatrix} \quad (2.78)$$

The last step needed to arrive at the A-parameters for the single layer medium is to combine (2.75) and (2.78), which results in

$$\begin{bmatrix} c_1 \\ b_1 \end{bmatrix} = \frac{1}{T_1} \begin{bmatrix} e^{\gamma_2 d_s} & \Gamma_1 e^{-\gamma_2 d_s} \\ \Gamma_1 e^{\gamma_2 d_s} & e^{-\gamma_2 d_s} \end{bmatrix} \begin{bmatrix} c_2 \\ b_2 \end{bmatrix} = \overbrace{\begin{bmatrix} A_{11} & A_{12} \\ A_{21} & A_{22} \end{bmatrix}}^{A\text{-parameters}} \begin{bmatrix} c_2 \\ b_2 \end{bmatrix} \quad (2.79)$$

In summary, (2.79) provides the A-parameters for the single layer configuration that relates the complex wave amplitudes of the forward and reverse waves at  $c_1$  and  $b_1$  to the complex wave amplitudes for the forward and reverse traveling waves at  $c_2$  and  $b_2$ .

### 2.2.2 A-Parameters for Multiple Layer Configuration.

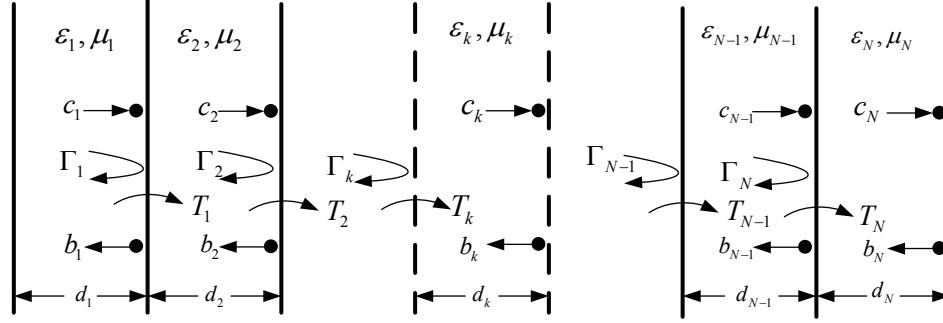


**Figure 2-3** Layout of Multiple Layer Configuration

By inspection, it is apparent that the complex wave amplitudes for the forward and reverse traveling waves at  $c_1$  and  $b_1$  can be related to  $c_N$  and  $b_N$  by simply cascading the A-parameter matrix derived in 2.2.1 as follows

$$\begin{bmatrix} c_1 \\ b_1 \end{bmatrix} = \prod_{k=1}^{N-1} \frac{1}{T_k} \begin{bmatrix} e^{\gamma_k d_k} & \Gamma_k e^{-\gamma_k d_k} \\ \Gamma_k e^{\gamma_k d_k} & e^{-\gamma_k d_k} \end{bmatrix} \begin{bmatrix} c_N \\ b_N \end{bmatrix} = \prod_{k=1}^{N-1} \begin{bmatrix} A_{11}^k & A_{12}^k \\ A_{21}^k & A_{22}^k \end{bmatrix} \begin{bmatrix} c_N \\ b_N \end{bmatrix} \quad (2.80)$$

$$\text{where: } \Gamma_k = \frac{Z_k - Z_{k-1}}{Z_k + Z_{k-1}} \text{ and } T_k = 1 + \Gamma_k$$



### **2.3 Summary**

This chapter provided a thorough understanding of rectangular waveguide theory and wave transmission matrices (a.k.a. A-parameters). Comprehensive knowledge of both concepts will form the foundation needed to successfully apply the modal-analysis technique to the problem stated in chapter one. Because the rectangular waveguide used for this thesis is reduced in two dimensions, higher-order  $TE$  and  $TM$  modes will be excited and scattered in all regions of the test apparatus, hence the need for the derived  $TE$  and  $TM$  field equations provided in (2.47) thru (2.52) and (2.59) thru (2.64). Regardless of the number of layers in the sample region, the derived A-parameters provide a straight-forward process to accommodate wave transmission through the reduced aperture sample holder region for the low-frequency.

2. Background.....	2-1
2.1 TE and TM Modes of a Rectangular Waveguide.....	2-1
2.1.1 Maxwell’s Equations.....	2-3
2.1.2 Helmholtz Wave Equation.....	2-5
2.1.3 Helmholtz Wave Equation Applied to Rectangular Waveguide.....	2-6
2.1.4 Separation of Variables.....	2-8
2.1.5 Application of Waveguide’s Boundary Conditions.....	2-11
2.1.6 Order of Modes Determined by Cut-off Frequency.....	2-16
2.2 Wave Transmission Matrices (A-Parameters).....	2-18
2.2.1 A-parameters for Single Layer Configuration.....	2-19
2.2.2 A-Parameters for Multiple Layer Configuration.....	2-22
2.3 Summary.....	2-23

<b>Figure 2-1</b> Cross-sectional dimensions of the rectangular waveguide .....	2-2
---	-----

<b>Figure 2-2</b> Layout of single layer material with reflected waves and transmitted waves .....	2-19
--	------

<b>Figure 2-3</b> Layout of Multiple Layer Configuration.....	2-22
---	------

### 3. Methodology

Using the previously derived *TE* fields, *TM* fields, and A-parameters, this chapter will conduct a rigorous modal analysis that directly aids in extracting the complex permittivity and permeability of a test sample placed inside a 2-D reduced aperture sample holder.

Using an initial guess of the test sample's constitutive parameters, theoretical S-parameters ( $S_{11}^{thy}$ ,  $S_{12}^{thy}$ ,  $S_{21}^{thy}$ , and  $S_{22}^{thy}$ ) will be calculated using the modal analysis solution and compared to experimental S-parameters ( $S_{11}^{meas}$ ,  $S_{12}^{meas}$ ,  $S_{21}^{meas}$ , and  $S_{22}^{meas}$ ) measured using a Hewlett-Packard 8510B Network Analyzer. If the theoretical S-parameters do not match the measured S-parameters to a specified accuracy, the complex permittivity and/or complex permeability will be adjusted using a non-linear least squares root searching algorithm, theoretical S-parameters will be re-calculated, and results compared to the experimental S-parameters again. This iterative process will continue until the theoretical S-parameters match the measured S-parameters within pre-defined limits. Once the least square error is less than the pre-defined accuracy, the respective complex permittivity and permeability are identified as the constitutive parameters for the test sample at that particular frequency.

The modal analysis used for this solution can be divided into three distinct tasks as follows: 1) expand the fields for each region, 2) satisfy boundary conditions across each interface, and 3) test with appropriate integral operators. The end-product of the modal analysis will be the theoretical S-parameters.

### 3.1 Field Expansions

The waveguide's reduced aperture dimensions and location (see Fig 3.1) were chosen to simplify the mode-matching process across the waveguide to sample holder interfaces at  $z = 0$  and  $z = d_N = d_{holder}$ . Matching the reduced aperture's aspect ratio to the waveguide's aspect ratio and centering the reduced aperture on the transverse axes facilitated mode orthogonality. Centering the aperture on the waveguide's cross-section greatly decreased the complexity of the field expansions for the different  $TE$  and  $TM$  scattered modes and reduced the modal analysis inner-product calculations because of the resulting symmetry.

#### 3.1.1 2-D Stepped-Waveguide Geometry.

Consider the geometries of Figures 3.2 and 3.3 showing respective top and side views of the generic 2-D stepped-waveguide fixture configuration. As mentioned before and indicated in Figure 3.1, the 2-D stepped aperture origin is placed in the cross-sectional center of the waveguide to simplify mathematical analysis. Region  $A$  exists where  $z < 0$ , has width  $a$ , height  $b$ , and is filled with air, implying the region's constitutive parameters are  $\epsilon_o, \mu_o$ . Region  $B$  shares the same physical dimensions and contents as Region  $A$ , but exists for  $z > d_N$ . The space between regions  $A$  and  $B$  is considered the sample region, has a reduced width  $w$  where  $w \leq a$ , reduced height  $h$  where  $h \leq b$ , and in general, is comprised of multiple material layers (only one layer is considered unknown). Adding the thickness of each layer in the sample region, including

the free-space layers, must span the total sample holder thickness. Mathematically, this is expressed as

$$d_N = d_{holder} = \sum_{i=1}^N d_i \quad (3.1)$$

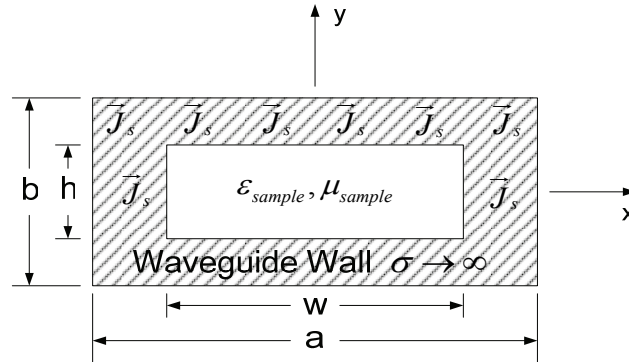


**Figure 3-1** Cross-sectional view of 2-D stepped waveguide fixture looking at the  $z = 0$  interface. Symbols  $\vec{J}_s$  identify excited surface currents caused by the incident  $TE_{10}$  wave.

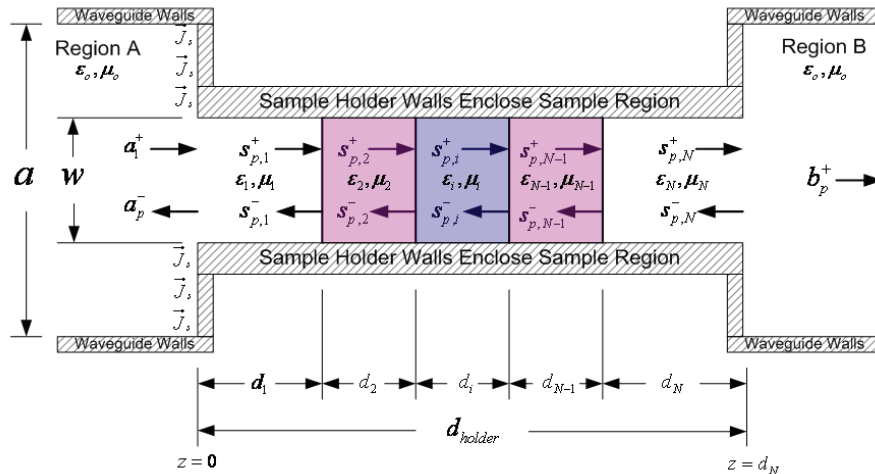


**Figure 3-2** Top view of 2-D reduced aperture waveguide fixture having one unknown layer (i.e. center) and multiple known layers. This arrangement presents a generic view that encompasses all possible sample holder configurations. Sample holder width exaggerated to adequately detail sample region. Symbols  $\vec{J}_s$  identify excited surface currents caused by incident  $TE_{10}$  wave.

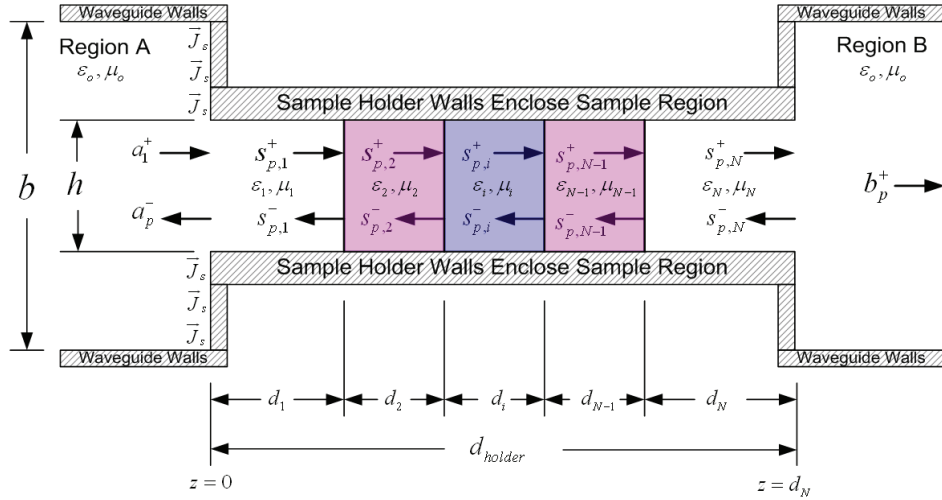


**Figure 3-3** Side view of 2-D reduced aperture waveguide fixture having one unknown layer (i.e. center) and multiple known layers.

### 3.1.2 Derivation of Higher-Order Scattered Fields.

As indicated in Figures 3.2 and 3.3, there exists a positive traveling  $TE_{10}$  wave with complex amplitude  $a_1^+$  incident upon the  $z = 0$  interface in Region A. The incident wave subsequently induces surface currents on the transverse surface areas labeled as  $\vec{J}_s$ , which produce higher-order modes that propagate in all regions of the test fixture.

The field components for the incident  $TE_{10}$  wave, with the aid of (2.47) thru (2.52), are

$$h_{x,10}^A(\vec{\rho}, z) = A_{10}^+ \frac{\gamma_{10}^A k_{x,1}^A}{(k_{c,10}^A)^2} \sin k_{x,1}^A \left( x + \frac{a}{2} \right) e^{-\gamma_{10}^A z} \quad (3.2)$$

$$h_{y,mn}(\vec{\rho}, z) = 0 \quad (3.3)$$

$$h_{z,10}^A(\vec{\rho}, z) = A_{10}^+ \cos k_{x,1}^A \left( x + \frac{a}{2} \right) \left( e^{-\gamma_{10}^A z} \right) \quad (3.4)$$

$$e_{x,mn}(\vec{\rho}) = 0 \quad (3.5)$$

$$e_{y,10}^A(\vec{\rho}, z) = -A_{10}^+ \frac{j\omega\mu_o k_{x,1}^A}{(k_{c,10}^A)^2} \sin k_{x,1}^A \left( x + \frac{a}{2} \right) e^{-\gamma_{10}^A z} \quad (3.6)$$

$$e_z(\vec{\rho}) = 0 \quad (3.7)$$

Inspection of (3.2) and (3.6), reveals that the non-zero transverse components ( $e_{y,10}^A$  and  $h_{x,10}^A$ ) of the  $TE_{10}$  mode are  $y$ -invariant and even about the center width of the waveguide ( $x = 0$ ). Since the structure and excitation are also even about the center, only *even*  $TE$  and  $TM$  scattered modes will be excited. This is *the* key assumption used to derive all higher-order, scattered,  $TE$  and  $TM$  field configurations. Note, verifying that the  $TE_{10}$  field incident on the  $z = 0$  interface is orthogonal to the derived scattered fields validates this assumption and is accomplished in Section 3.1.3.

For higher-order  $TE$  modes scattered in Region A, (2.51) provides  $e_{y,mn}^{TE}$ , which is repeated in (3.8) for reader convenience.

$$e_{y,mn}^{TE,A}(\vec{\rho}) = -A_{mn}^- \frac{j\omega\mu_o k_{x,m}^A}{(k_{c,mn}^A)^2} \sin k_{x,m}^A \left( x + \frac{a}{2} \right) \cos k_{y,n}^A \left( y + \frac{b}{2} \right) e^{\gamma_{m,n}^A z} \quad (3.8)$$

The sine term in (3.8) makes  $e_{y,mn}^{TE,A}$  odd if  $m$  is even (i.e. 0, 2, 4, ...) and the cosine term makes  $e_{y,mn}^{TE,A}$  odd for odd values of  $n$  (i.e. 1, 3, 5, ...). This is apparent by inspecting the trigonometric identities provided in (3.9) thru (3.12).

$$\sin k_{x,m} \left( x + \frac{a}{2} \right) = \begin{cases} (-1)^{\frac{m-1}{2}} \cos(k_{x,m}x) & \dots m = 1, 3, 5, \dots \text{odd} \\ (-1)^{\frac{m}{2}} \sin(k_{x,m}x) & \dots m = 2, 4, 6, \dots \text{even} \end{cases} \quad (3.9)$$

$$\cos k_{y,n} \left( y + \frac{b}{2} \right) = \begin{cases} (-1)^{\frac{n+1}{2}} \sin(k_{y,n}y) & \dots n = 1, 3, 5, \dots \text{odd} \\ (-1)^{\frac{n}{2}} \cos(k_{y,n}y) & \dots n = 0, 2, 4, \dots \text{even} \end{cases} \quad (3.11)$$

$$\cos k_{y,n} \left( y + \frac{b}{2} \right) = \begin{cases} (-1)^{\frac{n}{2}} \cos(k_{y,n}y) & \dots n = 0, 2, 4, \dots \text{even} \end{cases} \quad (3.12)$$

Judicious selection of the even cosine equalities provided in (3.9) and (3.12), accompanied with a little algebra reduces (3.8) to

$$e_{y,mn}^{TE,A^-} = (-1)^{\frac{m+n+1}{2}} \frac{j\omega\mu_o k_{x,m}^A}{(k_{c,mn}^A)^2} \cos(k_{x,m}^A x) \cos(k_{y,n}^A y) e^{\gamma_{m,n}^A z} \quad (3.13)$$

where  $m = 1, 3, 5, \dots \text{odd}$ , and  $n = 0, 2, 4, \dots \text{even}$

Using a similar analysis,  $e_{x,mn}^{TE,A^-}$  can be written as

$$e_{x,mn}^{TE,A^-} = (-1)^{\frac{m+n+1}{2}} \frac{j\omega\mu_o k_{y,n}^A}{(k_{c,mn}^A)^2} \sin(k_{x,m}^A x) \sin(k_{y,n}^A y) e^{\gamma_{m,n}^A z} \quad (3.14)$$

Combining (3.13) and (3.14) forms the total  $TE$  scattered electric field for Region A, which is

$$\vec{E}_{mn}^{TE,A^-} = \frac{(-1)^{\frac{m+n+1}{2}} j\omega\mu_o}{(k_{c,mn}^A)^2} \left\{ \hat{x} \left[ k_{y,n}^A \sin(k_{x,m}^A x) \sin(k_{y,n}^A y) \right] + \hat{y} \left[ k_{x,m}^A \cos(k_{x,m}^A x) \cos(k_{y,n}^A y) \right] \right\} e^{\gamma_{m,n}^A z} \quad (3.15)$$

The total  $TE$  scattered magnetic field for Region A is found by transforming (2.26) into

$$\vec{h}_i(\vec{\rho}) = \frac{\hat{z} \times \vec{e}_i(\vec{\rho})}{Z_{TE}} \quad (3.16)$$



which applied to  $\vec{E}_{mn}^{TE,A^-}$  yields

$$\vec{H}_{mn}^{TE,A^-} = \frac{\hat{z} \times \vec{E}_{mn}^{TE,A^-}}{Z_{TE,mn}^A} = \frac{(-1)^{\frac{m+n+1}{2}} j\omega\mu_o}{Z_{TE,mn}^A (k_{c,mn}^A)^2} \left\{ \begin{array}{l} \hat{x} k_{x,m}^A \cos(k_{x,m}^A x) \cos(k_{y,n}^A y) - \\ \hat{y} k_{y,n}^A \sin(k_{x,m}^A x) \sin(k_{y,n}^A y) \end{array} \right\} e^{\gamma_{mn}^A z} \quad (3.17)$$

where

$$k_{x,m}^A = \frac{m\pi}{a}, m = 1, 3, 5 \dots \text{odd}, k_{y,n}^A = \frac{n\pi}{b}, n = 0, 2, 4 \dots \text{even},$$

$$(k_{c,mn}^A)^2 = (k_{x,m}^A)^2 + (k_{y,n}^A)^2, \text{ and } \gamma_{mn}^A = \sqrt{(k_{c,mn}^A)^2 - k_o^2}$$

As mentioned earlier, the scattered higher-order fields produced by excited surface currents at  $z = 0$  interface will be both  $TE$  and  $TM$ . So,  $e_{y,rs}^{TM,A^-}$  from the scattered  $TM$  electric field must also be reduced to maintain evenness about  $x = 0$ . For reader convenience  $e_{y,rs}^{TM,A^-}$  has been repeated from (2.60) to (3.18).

$$e_{y,rs}^{TM,A^-}(\vec{\rho}, z) = -D_{rs}^- \frac{\gamma_{rs}^A k_{y,r}^A}{(k_{c,rs}^A)^2} \sin k_{x,r}^A \left( x + \frac{a}{2} \right) \cos k_{y,s}^A \left( y + \frac{b}{2} \right) e^{\gamma_{rs}^A z} \quad (3.18)$$

The sine and cosine terms in (3.18) are identical in form to the sine and cosine terms in (3.8) except that  $m$  and  $r$ , and  $n$  and  $s$  are interchanged. This means the same trigonometric identities from (3.9) and (3.12) can be substituted into (3.18) to make  $e_{y,rs}^{TM,A^-}$  an even function about  $x = 0$  as indicated in (3.19).

$$e_{y,rs}^{TM,A^-}(\vec{\rho}, z) = \frac{(-1)^{\frac{r+s+1}{2}} \gamma_{rs}^A k_{y,s}^A}{(k_{c,rs}^A)^2} \cos(k_{x,r}^A x) \cos(k_{y,s}^A y) e^{\gamma_{rs}^A z} \quad (3.19)$$

where

$$k_{x,r}^A = \frac{r\pi}{a} \dots r = 1, 3, 5 \dots \text{odd}, k_{y,s}^A = \frac{s\pi}{b} \dots s = 2, 4, 6 \dots \text{even}$$

$$\gamma_{rs}^A = \sqrt{(k_{c,rs}^A)^2 - k_o^2}, k_o = \frac{\omega}{c}, \text{ and } (k_{c,rs}^A)^2 = (k_{x,r}^A)^2 + (k_{y,s}^A)^2$$

Using a similar analysis,  $e_{x,rs}^{TM,A^-}$  can be written as

$$e_{x,rs}^{TM,A^-}(\vec{\rho}, z) = -(-1)^{\frac{r+s+1}{2}} \frac{\gamma_{rs}^A k_{x,r}^A}{(k_{c,rs}^A)^2} \sin(k_{x,r}^A x) \sin(k_{y,s}^A y) e^{\gamma_{rs}^A z} \quad (3.20)$$

Now that all of the even  $TM$  electric field components are derived, (3.19) and (3.20) are combined to form the total, reverse propagating, scattered,  $TM$  electric field.

$$\vec{E}_{rs}^{TM,A^-} = \frac{(-1)^{\frac{r+s+1}{2}} \gamma_{rs}^A}{(k_{c,rs}^A)^2} \left\{ \begin{array}{l} -\hat{x} k_{x,r}^A \sin(k_{x,r}^A x) \sin(k_{y,s}^A y) + \\ \hat{y} k_{y,s}^A \cos(k_{x,r}^A x) \cos(k_{y,s}^A y) \end{array} \right\} e^{\gamma_{rs}^A z} \quad (3.21)$$

The total  $TM$  scattered magnetic field for Region A is found by applying (2.28), which yields

$$\vec{H}_{rs}^{TM,A^-} = \frac{(-1)^{\frac{r+s+1}{2}} \gamma_{rs}^A}{Z_{TM,rs}^A (k_{c,rs}^A)^2} \left\{ \begin{array}{l} \hat{x} k_{y,s}^A \cos(k_{x,r}^A x) \cos(k_{y,s}^A y) + \\ \hat{y} k_{x,r}^A \sin(k_{x,r}^A x) \sin(k_{y,s}^A y) \end{array} \right\} e^{\gamma_{rs}^A z} \quad (3.22)$$

### 3.1.3 Mode Orthogonality

Note that the physical insight leading to consideration of only this limited set of higher-order modes can be supported through mode orthogonality. That is, integrating the dot product of the incident  $TE_{10}$  electric field with the electric fields presented in (3.15) and (3.21) over the cross-section of the sample holder aperture should yield results other than zero if the fields are electromagnetically coupled. If the dot product of the incident field with a scattered electric field yields zero, it implies that the fields are not electromagnetically coupled. To begin, consider integrating the dot product of the incident  $TE_{10}$  electric field ( $\vec{E}_{10}^{TE,A^+}$ ) with  $\vec{E}_{mn}^{TE,A^-}$  presented in (3.15) over the aperture transverse area as expressed in (3.23).

$$\int_{-b/2}^{b/2} \int_{-w/2}^{w/2} \vec{E}_{10}^{TE,A^+} \cdot \vec{E}_{mn}^{TE,A^-} dx dy, \quad m = 1, 3, 5, \dots, \quad n = 0, 2, 4, \dots \quad (3.23)$$

Dropping the constants and grouping terms inside their respective integrals leads to

$$\int_{-w/2}^{w/2} \cos(k_{x,1}^A x) \cos(k_{x,m}^A x) dx \int_{-b/2}^{b/2} \cos(k_{y,n}^A y) dy \neq 0 \quad (3.24)$$

where:  $m = 1, 3, 5, \dots$ ,  $n = 0, 2, 4, \dots$

This provides a pair of even functions integrated over symmetric limits yielding a non-zero result. The only other mode selections possible for the scattered electric field are  $m = 2, 4, 6, \dots, \text{even}$  and/or  $n = 1, 3, 5, \dots, \text{odd}$ . If  $m = 2, 4, 6, \dots, \text{even}$ , (3.24) becomes

$$\int_{-w/2}^{w/2} \cos(k_{x,1}^A x) \sin(k_{x,m}^A x) dx \int_{-b/2}^{b/2} \cos(k_{y,n}^A y) dy = 0 \quad (3.25)$$

And, if  $n = 1, 3, 5, \dots, \text{odd}$  (3.24) becomes

$$\int_{-w/2}^{w/2} \cos(k_{x,1}^A x) \cos(k_{x,m}^A x) dx \int_{-b/2}^{b/2} \sin(k_{y,n}^A y) dy = 0 \quad (3.26)$$

Equations (3.25) and (3.26) both integrate to zero because odd, un-shifted sine functions within an integral having symmetric limits are always zero. Therefore, the only modes that successfully couple into the sample holder region will be modes containing index pairs (i.e.  $m$  and  $n$ ) such that  $m = 1, 3, 5, \dots, \text{odd}$ ,  $n = 0, 2, 4, \dots, \text{even}$ .

### 3.1.4 Field Expansions in Waveguide Regions.

The transverse fields in waveguide regions A and B are given by the following expansions

$$\left. \begin{aligned} \vec{E}_t^A &= A_1^+ \vec{e}_1^A e^{-\gamma_1^A z} + \sum_{p=1}^P A_p^- \vec{e}_p^A e^{\gamma_p^A z} \\ \vec{H}_t^A &= A_1^+ \vec{h}_1^A e^{-\gamma_1^A z} - \sum_{p=1}^P A_p^- \vec{h}_p^A e^{\gamma_p^A z} \end{aligned} \right\} \dots z < 0 \text{ (Region A)} \quad (3.27)$$

$$\left. \begin{aligned} \vec{E}_t^B &= \sum_{p=1}^P B_p^+ \vec{e}_p^B e^{-\gamma_p^B (z-d_N)} \\ \vec{H}_t^B &= \sum_{p=1}^P B_p^+ \vec{h}_p^B e^{-\gamma_p^B (z-d_N)} \end{aligned} \right\} \dots z > d_N \text{ (Region B)} \quad (3.28)$$

where  $A_1^+$  is the complex amplitude of the incident  $TE_{10}$  mode traveling in the +z-direction in region A.  $A_p^-$  is the complex amplitude of the  $p^{\text{th}}$  mode reflected from the waveguide to sample holder interface at  $z=0$  traveling in the -z-direction. Similarly,  $B_p^+$  is the complex amplitude of the  $p^{\text{th}}$  mode transmitted through the sample region into region B traveling in the +z-direction.

The variable  $p$  in (3.27) and (3.28) designates the mode indices (i.e.  $m=1$ ,  $n=2$  for  $TE$  or  $r=1$ ,  $s=2$  for  $TM$ ) and dictates the type of field (i.e.  $TE$  or  $TM$ ). As explained in Chapter 2, the order of the modes depends on the waveguide's transverse aspect ratio. For this thesis, an S-band waveguide was used where the transverse height and width are 1.34 inches and 2.84 inches respectively. It was assumed that if a  $TE_{mn}$  mode existed where  $n \neq 0$ , there coexisted a  $TM_{rs}$  mode where  $m=r$  and  $n=s$ . A

$TM_{r,0}$  mode with  $m = r$  cannot coexist because  $s$  can never be zero as explained in Chapter 2. For the field configurations derived in Section 3.1.2, the first five scattered  $TE$  modes existing in the S-band waveguide are:  $TE_{10}$ ,  $TE_{30}$ ,  $TE_{12}$ ,  $TE_{50}$ , and  $TE_{32}$ .

Within these first five  $TE$  modes, there coexists a  $TM_{12}$  and  $TM_{32}$  mode as well.

Merging the  $TE$  and  $TM$  modes together to form an ordered list of modes yields:  $TE_{10}$ ,  $TE_{30}$ ,  $TE_{12}$ ,  $TM_{12}$ ,  $TE_{50}$ ,  $TE_{32}$ , and  $TM_{32}$ . This list of indices formed by merging  $TE$  and  $TM$  modes together in order was defined as the “ $p$ ” modes seen in (3.27) and (3.28). For example,  $p = 1$  identifies the  $TE_{10}$  mode and  $p = 4$  identifies the  $TM_{12}$  mode. Now that the  $p$  modes are fully explained, the transverse electric fields in (3.27) and (3.28) are extracted from (3.15) and (3.21), and provided in (3.29) thru (3.31) respectively.

$$\vec{e}_1^A = -\hat{y} \frac{j\omega\mu_o}{k_{x,1}^A} \cos(k_{x,1}^A x) \dots \text{for } TE_{10} \quad (3.29)$$

$$\vec{e}_p^A = \vec{e}_p^B = \left\{ \begin{array}{l} \hat{x} [k_{y,n}^A \sin(k_{x,m}^A x) \sin(k_{y,n}^A y)] + \\ \hat{y} [k_{x,m}^A \cos(k_{x,m}^A x) \cos(k_{y,n}^A y)] \end{array} \right\} \dots \text{for } TE \quad (3.30)$$

$$\vec{e}_p^A = \vec{e}_p^B = \left\{ \begin{array}{l} -\hat{x} k_{x,r}^A \sin(k_{x,r}^A x) \sin(k_{y,s}^A y) + \\ \hat{y} k_{y,s}^A \cos(k_{x,r}^A x) \cos(k_{y,s}^A y) \end{array} \right\} \dots \text{for } TM \quad (3.31)$$

Because the term  $\frac{(-1)^{\frac{m+n+1}{2}} j\omega\mu_o}{(k_{c,mn}^A)^2}$  from (3.15) and (3.17) is common to  $TE$  transverse

electric and magnetic fields, it can be dropped from both  $TE$  field equations (2.15) and (2.17).

Another way to justify dropping this term is to multiply both sides of (2.24) by

$$\frac{(k_{c,mn}^A)^2}{(-1)^{\frac{m+n+1}{2}} j\omega\mu_o}. \text{ The resulting } TE \text{ generating function provided in (2.36) would have}$$

$$\frac{(k_{c,mn}^A)^2}{(-1)^{\frac{m+n+1}{2}} j\omega\mu_o} \text{ as a leading coefficient, which would eventually cancel with}$$

$$\frac{(-1)^{\frac{m+n+1}{2}} j\omega\mu_o}{(k_{c,mn}^A)^2}, \text{ the leading term for all } TE \text{ field components. When extending this same}$$

analysis to *TM* field components, the  $\frac{(-1)^{\frac{r+s+1}{2}} \gamma_{rs}^A}{(k_{c,rs}^A)^2}$  term can also be dropped. Therefore,

application of (3.16) yields

$$\vec{h}_1^A = \frac{\hat{z} \times \vec{e}_1^A}{Z_{TE,10}^A} \quad (3.32)$$

$$\vec{h}_p^A = \vec{h}_p^B = \frac{\hat{z} \times \vec{e}_p^{A,B}(\vec{\rho})}{Z_{TE,p}^{A,B}} \dots \text{for } TE \quad (3.33)$$

$$\vec{h}_p^A = \vec{h}_p^B = \frac{\hat{z} \times \vec{e}_p^A}{Z_{TM,p}^{A,B}} \dots \text{for } TM \quad (3.34)$$

where

$$Z_{TE,p}^{A,B} = \frac{j\omega\mu_o}{\gamma_p^{A,B}}, \quad Z_{TM,p}^{A,B} = \frac{\gamma_p^{A,B}}{j\omega\epsilon_o}$$

$$\gamma_p^{A,B} = \sqrt{(k_{c,p}^{A,B})^2 - k_o^2}$$

$$k_o = \frac{\omega}{c}, \text{ and } c = \frac{1}{\sqrt{\epsilon_o\mu_o}}$$

$\omega$  = angular frequency of incident wave

$$k_{x,m}^A = \frac{m\pi}{a} \dots m = 1, 3, 5 \dots \text{odd}$$

$$k_{y,n}^A = \frac{n\pi}{b} \dots n = 0, 2, 4 \dots \text{even}$$

$$k_{c,p}^A = \sqrt{(k_{x,m}^A)^2 + (k_{y,n}^A)^2} \dots \text{for TE modes}$$

$$k_{x,r}^A = \frac{r\pi}{a} \dots r = 1, 3, 5 \dots \text{odd}$$

$$k_{y,s}^A = \frac{s\pi}{b} \dots s = 2, 4, 6 \dots \text{even}$$

$$k_{c,p}^A = \sqrt{(k_{x,r}^A)^2 + (k_{y,s}^A)^2} \dots \text{for TM modes}$$

$$\gamma_p^A = \sqrt{(k_{c,p}^A)^2 - k_o^2} \dots \text{where } k_o = \frac{\omega}{c}$$

It is apparent that the number of higher-order *TE* and *TM* modes possible is infinite, but the number of modes required to arrive at an accurate representation of the fields in each region is dependent on the degree of waveguide reduction. As the aperture is reduced in cross-sectional area (i.e.  $w \rightarrow 0$  and  $h \rightarrow 0$ ), the number of modes needed to adequately represent the field increases (i.e.  $p \rightarrow \infty$ ). Conversely, when the aperture's dimensions are that of the waveguide (i.e.  $w = a$  and  $h = b$ ), the number of modes required is only one (i.e.  $p = 1$ ), the  $TE_{10}$  mode. This makes physical sense as the dominate mode in any rectangular waveguide without reduction is the  $TE_{10}$  mode.

### 3.1.5 Field Expansions in Sample Region.

In general, two layers will exist within the sample region at a minimum. As such, the sample region has been modeled based on a multi-layer configuration as illustrated in Figures 3.2 and 3.3. This modeling approach has another useful application. If the unknown test sample is not rigid enough to maintain a planar posture in the sample

holder, it must be “sandwiched” between two rigid dielectric materials to meet the planar requirement. Therefore, the multi-layer model provides an extra degree of manufacturing freedom (i.e. test sample thickness). The only caveat to this approach is that the constitutive parameters of each layer besides the test sample be known.

The transverse field equations in the  $i^{\text{th}}$  layer of the sample holder region are given by

$$\left. \begin{aligned} \vec{E}_t^{s,i} &= \sum_{p=1}^P s_{p,i}^+ \vec{e}_p^{s,i} e^{-\gamma_p^{s,i}(z-d_i)} + \sum_{p=1}^P s_{p,i}^- \vec{e}_p^{s,i} e^{\gamma_p^{s,i}(z-d_i)} \\ \vec{H}_t^{s,i} &= \sum_{p=1}^P s_{p,i}^+ \vec{h}_p^{s,i} e^{-\gamma_p^{s,i}(z-d_i)} - \sum_{p=1}^P s_{p,i}^- \vec{h}_p^{s,i} e^{\gamma_p^{s,i}(z-d_i)} \end{aligned} \right\} d_{i-1} < z < d_N \dots (\text{Sample Region}) \quad (3.35)$$

where the distance to each material's reference plane is determined by

$$d_i = \sum_{k=1}^i \ell_k \quad (3.36)$$

Variable  $s_{p,i}^{\pm}$  is the complex amplitude of the  $p^{\text{th}}$  mode at the  $i^{\text{th}}$  layer traveling in the  $\pm z$ -direction. The transverse electric and magnetic fields in the sample region are similar in form to the electric field in regions A & B and are provided in (3.37) thru (3.40).

$$\vec{e}_p^{s,i} = \left\{ \begin{aligned} &\hat{x} \left[ k_{y,n}^S \sin(k_{x,m}^S x) \sin(k_{y,n}^S y) \right] + \\ &\hat{y} \left[ k_{x,m}^S \cos(k_{x,m}^S x) \cos(k_{y,n}^S y) \right] \end{aligned} \right\} \dots \text{for } TE \quad (3.37)$$

$$\vec{e}_p^{s,i} = \left\{ \begin{aligned} &-\hat{x} k_{x,r}^S \sin(k_{x,r}^S x) \sin(k_{y,s}^S y) + \\ &\hat{y} k_{y,s}^S \cos(k_{x,r}^S x) \cos(k_{y,s}^S y) \end{aligned} \right\} \dots \text{for } TM \quad (3.38)$$

$$\vec{h}_p^{s,i} = \frac{\hat{z} \times \vec{e}_p^{s,i}}{Z_{TE,p}^{s,i}} \dots \text{for } TE \quad (3.39)$$



$$\vec{h}_p^{s,i} = \frac{\hat{z} \times \vec{e}_p^{s,i}}{Z_{TM,p}^{s,i}} \dots \text{for TM} \quad (3.40)$$

where

$$Z_{TE,p}^{s,i} = \frac{j\omega\mu_i}{\gamma_p^{s,i}}, \quad Z_{TM,p}^{s,i} = \frac{\gamma_p^{s,i}}{j\omega\epsilon_i}$$

$\epsilon_i$  = complex permittivity of the  $i^{\text{th}}$  layer

$\mu_i$  = complex permeability of the  $i^{\text{th}}$  layer

$\epsilon_{r,i}$  = relative complex permittivity of the  $i^{\text{th}}$  layer

$\mu_{r,i}$  = relative complex permeability of the  $i^{\text{th}}$  layer

$$k_i = \frac{\omega}{c} \sqrt{\epsilon_{r,i} \mu_{r,i}}$$

$$\gamma_p^{s,i} = \sqrt{(k_{c,p}^s)^2 - k_i^2}$$

$$k_{x,m}^s = \frac{m\pi}{w} \dots \text{where } m = 1, 3, 5 \dots \text{odd}$$

$$k_{y,n}^s = \frac{n\pi}{h} \dots \text{where } n = 0, 2, 4 \dots \text{even}$$

$$k_{c,p}^s = \sqrt{(k_{x,m}^s)^2 + (k_{y,n}^s)^2} \dots \text{for TE modes}$$

$$k_{x,r}^s = \frac{r\pi}{w} \dots \text{where } r = 1, 3, 5 \dots \text{odd}$$

$$k_{y,s}^s = \frac{s\pi}{h} \dots \text{where } s = 2, 4, 6 \dots \text{even}$$

$$k_{c,p}^s = \sqrt{(k_{x,r}^s)^2 + (k_{y,s}^s)^2} \dots \text{for TM modes}$$

### 3.2 Satisfying Boundary Conditions

The second task of the modal analysis process is to satisfy tangential boundary conditions across each interface (i.e.  $z = 0$  and  $z = d_N$ ). Enforcing continuity of the tangential fields across the sample holder interface at  $z = 0$  leads to

$$A_1^+ \bar{e}_1^A + \sum_{p=1}^P A_p^- \bar{e}_p^A = \begin{cases} \sum_{p=1}^P s_{p,1}^+ \bar{e}_p^{s,1} e^{\gamma_p^{s,1} d_1} + \sum_{p=1}^P s_{p,1}^- \bar{e}_p^{s,1} e^{-\gamma_p^{s,1} d_1} \dots \text{for } |x| < w, |y| < h \\ 0 \dots \text{for } -a/2 < x < -w/2, a/2 < x < w/2 \\ 0 \dots \text{for } -b/2 < y < -h/2, b/2 < y < h/2 \end{cases} \quad (3.41)$$

$$A_1^+ \bar{h}_1^A - \sum_{p=1}^P A_p^- \bar{h}_p^A = \sum_{p=1}^P s_{p,1}^+ \bar{h}_p^{s,1} e^{\gamma_p^{s,1} d_1} - \sum_{p=1}^P s_{p,1}^- \bar{h}_p^{s,1} e^{-\gamma_p^{s,1} d_1} \dots \text{for } |x| < w, |y| < h \quad (3.42)$$

Enforcing continuity of the tangential fields across the sample holder interface at  $z = d_N$

leads to

$$\sum_{p=1}^P B_p^+ \bar{e}_p^B = \begin{cases} \sum_{p=1}^P s_{p,N}^+ \bar{e}_p^{s,N} + \sum_{p=1}^P s_{p,N}^- \bar{e}_p^{s,N} \dots \text{for } |x| < w, |y| < h \\ 0 \dots \text{for } -a/2 < x < -w/2, a/2 < x < w/2 \\ 0 \dots \text{for } -b/2 < y < -h/2, b/2 < y < h/2 \end{cases} \quad (3.43)$$

$$\sum_{p=1}^P B_p^+ \bar{h}_p^B = \sum_{p=1}^P s_{p,N}^+ \bar{h}_p^{s,N} - \sum_{p=1}^P s_{p,N}^- \bar{h}_p^{s,N} \dots \text{for } |x| < w, |y| < h \quad (3.44)$$

Since the tangential electric field boundary condition is known (i.e.  $\vec{E}_{tang} = 0$ ) in the regions  $-a/2 < x < -w/2$ ,  $a/2 < x < w/2$ ,  $-b/2 < y < -h/2$ , and  $b/2 < y < h/2$  at  $z = 0$  and  $z = d_N$ , application of the uniqueness theorem makes it possible to satisfy only the magnetic field boundary condition only in the aperture cross-sectional area ( $|x| < w, |y| < h$ ).

Enforcement of tangential boundary conditions across each individual material interface within the sample region is not required as this feature is built into the wave

transmission analysis described in Chapter 2. Furthermore, due to the mode orthogonality that exists within the sample holder region, the amplitude coefficients at  $z = 0$  are related to those at  $z = d_N$  by

$$\begin{aligned}
\begin{bmatrix} s_{p,1}^+ \\ s_{p,1}^- \end{bmatrix} &= \prod_{i=2}^N \frac{1}{\tau_p^{s,i}} \begin{bmatrix} e^{\gamma_p^{s,i} d_i} & \Gamma_p^{s,i} e^{-\gamma_p^{s,i} d_i} \\ \Gamma_p^{s,i} e^{\gamma_p^{s,i} d_i} & e^{-\gamma_p^{s,i} d_i} \end{bmatrix} \begin{bmatrix} s_{p,N}^+ \\ s_{p,N}^- \end{bmatrix} \\
&= \begin{bmatrix} A_{11}^p & A_{12}^p \\ A_{21}^p & A_{22}^p \end{bmatrix} \begin{bmatrix} s_{p,N}^+ \\ s_{p,N}^- \end{bmatrix} \\
\Rightarrow s_{p,1}^+ &= A_{11}^p s_{p,N}^+ + A_{12}^p s_{p,N}^- \\
\Rightarrow s_{p,1}^- &= A_{21}^p s_{p,N}^+ + A_{22}^p s_{p,N}^-
\end{aligned} \tag{3.45}$$

where

$$\Gamma_p^{s,i} = \frac{Z_p^{s,i} - Z_p^{s,i-1}}{Z_p^{s,i} + Z_p^{s,i-1}}, \quad \tau_p^{s,i} = 1 + \Gamma_p^{s,i}$$

$$Z_p^{s,i} = \begin{cases} \frac{j\omega\mu_i}{\gamma_p^{s,i}} & \dots \text{for TE} \\ \frac{\gamma_p^{s,i}}{j\omega\varepsilon_i} & \dots \text{for TM} \end{cases}, \quad \text{and } \gamma_p^{s,i} = \sqrt{(k_{c,p}^s)^2 - k_i^2}$$

This relationship was developed from (2.80) with  $s_{p,i}^+$ ,  $s_{p,i}^-$ ,  $s_{p,N}^+$ , and  $s_{p,N}^-$  substituted for  $c_1$ ,  $b_1$ ,  $c_N$ , and  $b_N$  respectively. It is important to note that each mode (i.e.  $TE_{10}$ ,  $TE_{30}$ ,  $TM_{12}$ , or  $TM_{32}$ ) will electromagnetically couple independently to the same mode across each material inside the sample holder without disturbing other modes. This assumption is based on mode orthogonality and observing the sample holder's geometry is unchanged throughout its width.

$s_{p,1}^+$  and  $s_{p,1}^-$  can be expressed in terms of  $s_{p,N}^+$  and  $s_{p,N}^-$  via A-parameters, and their respective equations from (3.45) can be substituted into (3.41) and (3.42). After direct substitution and some algebraic manipulation, the following equations result

$$A_1^+ \vec{e}_1^A + \sum_{p=1}^P A_p^- \vec{e}_p^A = \sum_{p=1}^P s_{p,N}^+ \left[ A_{11}^p e^{\gamma_p^{s,1} d_1} + A_{21}^p e^{-\gamma_p^{s,1} d_1} \right] \vec{e}_p^{s,1} + \sum_{p=1}^P s_{p,N}^- \left[ A_{12}^p e^{\gamma_p^{s,1} d_1} + A_{22}^p e^{-\gamma_p^{s,1} d_1} \right] \vec{e}_p^{s,1} \quad (3.46)$$

$$A_1^+ \vec{h}_1^A - \sum_{p=1}^P A_p^- \vec{h}_p^A = \sum_{p=1}^P s_{p,N}^+ \left[ A_{11}^p e^{\gamma_p^{s,1} d_1} - A_{21}^p e^{-\gamma_p^{s,1} d_1} \right] \vec{h}_p^{s,1} + \sum_{p=1}^P s_{p,N}^- \left[ A_{12}^p e^{\gamma_p^{s,1} d_1} - A_{22}^p e^{-\gamma_p^{s,1} d_1} \right] \vec{h}_p^{s,1} \quad (3.47)$$

Dividing both sides of (3.43), (3.44), (3.46), and (3.47) by  $A_1^+$  and letting

$$R_p = \frac{A_p^-}{A_1^+} \dots \text{reflection coefficient at } z = 0 \text{ interface} \quad (3.48)$$

$$T_p = \frac{s_{p,N}^+}{A_1^+} \dots \text{transmission coefficient at } z = d_N \text{ interface} \quad (3.49)$$

$$r_p = \frac{s_{p,N}^-}{A_1^+} \dots \text{reflection coefficient at } z = d_N \text{ interface} \quad (3.50)$$

$$t_p = \frac{B_p^+}{A_1^+} \dots \text{transmission coefficient at } z = d_N \text{ interface} \quad (3.51)$$

yields,

$$\vec{e}_1^A + \sum_{p=1}^P R_p \vec{e}_p^A = \sum_{p=1}^P T_p \left[ A_{11}^p e^{\gamma_p^{s,1} d_1} + A_{21}^p e^{-\gamma_p^{s,1} d_1} \right] \vec{e}_p^{s,1} + \sum_{p=1}^P r_p \left[ A_{12}^p e^{\gamma_p^{s,1} d_1} + A_{22}^p e^{-\gamma_p^{s,1} d_1} \right] \vec{e}_p^{s,1} \quad (3.52)$$

$$\vec{h}_1^A - \sum_{p=1}^P R_p \vec{h}_p^A = \sum_{p=1}^P T_p \left[ A_{11}^p e^{\gamma_p^{s,1} d_1} - A_{21}^p e^{-\gamma_p^{s,1} d_1} \right] \vec{h}_p^{s,1} + \sum_{p=1}^P r_p \left[ A_{12}^p e^{\gamma_p^{s,1} d_1} - A_{22}^p e^{-\gamma_p^{s,1} d_1} \right] \vec{h}_p^{s,1} \quad (3.53)$$

$$\sum_{p=1}^P t_p \vec{e}_p^B = \sum_{p=1}^P T_p \vec{e}_p^{s,N} + \sum_{p=1}^P r_p \vec{e}_p^{s,N} \quad (3.54)$$

$$\sum_{p=1}^P t_p \vec{h}_p^B = \sum_{p=1}^P T_p \vec{h}_p^{s,N} - \sum_{p=1}^P r_p \vec{h}_p^{s,N} \quad (3.55)$$

Equations (3.52) thru (3.55) represent four linearly independent equations, each possessing four unknown ratios ( $R_p$ ,  $T_p$ ,  $r_p$ , and  $t_p$ ). But, each equation has  $P$  (number of modes considered) occurrences, which equates to  $4P$  unknowns. Therefore, to make this system of equations “well-behaved,” there must be  $4P$  equations to adequately solve for the  $4P$  unknowns.

### 3.3 Testing with Integral Operators

As stated in the previous section, there must exist  $4P$  linearly independent equations to solve for the  $4P$  unknown ratios ( $R_p$ ,  $T_p$ ,  $r_p$ , and  $t_p$ ). In order to generate  $4P$  linearly independent equations, testing operators were selected based on mode orthogonality. For example, the electric field testing function in (3.56) is orthogonal to the electric fields in all waveguide regions. Similarly, the magnetic field testing function in (3.57) is orthogonal to the magnetic fields in all the waveguide regions. The testing functions were then applied to (3.52) thru (3.55).

$$\int_{-b/2}^{b/2} \int_{-a/2}^{a/2} \bar{\mathbf{e}}_l^A \cdot \{ \} dx dy \quad , \quad l=1,2,3...P \quad (3.56)$$

$$\text{where: } \bar{\mathbf{e}}_l^A = \begin{cases} \hat{x} k_{y,n}^A \sin(k_{x,m}^A x) \sin(k_{y,n}^A y) + \hat{y} k_{x,m}^A \cos(k_{x,m}^A x) \cos(k_{y,n}^A y) & \dots \text{for } TE \\ -\hat{x} k_{x,r}^A \sin(k_{x,r}^A x) \sin(k_{y,s}^A y) + \hat{y} k_{y,s}^A \cos(k_{x,r}^A x) \cos(k_{y,s}^A y) & \dots \text{for } TM \end{cases}$$

and,

$$Z_{TM,l}^{s,i} \int_{-b/2}^{h/2} \int_{-w/2}^{w/2} \bar{\mathbf{h}}_l^s \cdot \{ \} dx dy \quad , \quad l=1,2,3...P \quad (3.57)$$

$$\text{where } \bar{\mathbf{h}}_l^s = \begin{cases} \frac{\hat{z} \times \bar{\mathbf{e}}_l^S}{Z_{TE,l}^{s,i}} & \dots \text{for } TE \\ \frac{\hat{z} \times \bar{\mathbf{e}}_l^S}{Z_{TM,l}^{s,i}} & \dots \text{for } TM \end{cases}$$

It is important to note that the testing functions  $\bar{\mathbf{e}}_l^A$  and  $\bar{\mathbf{h}}_l^s$  could be either *TE* or *TM* depending on the index  $l$ . Index  $l$  is similar to index  $p$  as explained in Section 3.1.3 such that  $l$  refers to the same ordered modes as  $p$ . For example, given the set of modes ordered as  $TE_{10}$ ,  $TE_{30}$ ,  $TE_{12}$ ,  $TM_{12}$ ,  $TE_{50}$ ,  $TE_{32}$ , and  $TM_{32}$ ,  $l=1$  implies selection of the  $TE_{10}$  mode just as  $l=4$  selects the  $TM_{12}$  mode. Having said this, the four possible mode combinations of inner-products within each testing operator are  $TE \bullet TE$ ,  $TE \bullet TM$ ,  $TM \bullet TE$ , and  $TM \bullet TM$ .

Equation generation occurs when (3.52) and (3.54) are each separately inserted into (3.56), and (3.53) and (3.55) are each separately inserted into (3.57). This insertion transforms (3.52) thru (3.55) into

$$\begin{aligned}
& \overbrace{\int_0^{b/2} \int_0^{a/2} \vec{e}_l^A \cdot \vec{e}_1^A dx dy}^{=C_{l1}} + \sum_{p=1}^P \overbrace{R_p \int_0^{b/2} \int_0^{a/2} \vec{e}_l^A \cdot \vec{e}_p^A dx dy}^{=C_{lp}} = \\
& \sum_{p=1}^P T_p \left[ A_{11}^p e^{\gamma_p^{s,1} d_1} + A_{21}^p e^{-\gamma_p^{s,1} d_1} \right] \overbrace{\int_0^{b/2} \int_0^{a/2} \vec{e}_l^A \cdot \vec{e}_p^{s,1} dx dy}^{=D_{lp}^{z=0}} + \\
& \sum_{p=1}^P r_p \left[ A_{12}^p e^{\gamma_p^{s,1} d_1} + A_{22}^p e^{-\gamma_p^{s,1} d_1} \right] \overbrace{\int_0^{b/2} \int_0^{a/2} \vec{e}_l^A \cdot \vec{e}_p^{s,1} dx dy}^{=D_{lp}^{z=0}}
\end{aligned} \tag{3.58}$$

where  $l = 1, 2, 3 \dots P$

$$\begin{aligned}
& \overbrace{Z_{TM,l}^{s,i} \int_0^{b/2} \int_0^{w/2} \vec{h}_l^s \cdot \vec{h}_1^A dx dy}^{=F_{l1}} - \sum_{p=1}^P \overbrace{R_p Z_{TM,l}^{s,i} \int_0^{h/2} \int_0^{w/2} \vec{h}_l^s \cdot \vec{h}_p^A dx dy}^{=F_{lp}} = \\
& \sum_{p=1}^P T_p \left[ A_{11}^p e^{\gamma_p^{s,1} d_1} - A_{21}^p e^{-\gamma_p^{s,1} d_1} \right] \overbrace{Z_{TM,l}^{s,i} \int_0^{h/2} \int_0^{w/2} \vec{h}_l^s \cdot \vec{h}_p^{s,1} dx dy}^{=Q_{lp}} + \\
& \sum_{p=1}^P r_p \left[ A_{12}^p e^{\gamma_p^{s,1} d_1} - A_{22}^p e^{-\gamma_p^{s,1} d_1} \right] \overbrace{Z_{TM,l}^{s,i} \int_0^{h/2} \int_0^{w/2} \vec{h}_l^s \cdot \vec{h}_p^{s,1} dx dy}^{=Q_{lp}}
\end{aligned} \tag{3.59}$$

where  $l = 1, 2, 3 \dots P$

$$\sum_{p=1}^P \overbrace{t_p \int_0^{b/2} \int_0^{a/2} \vec{e}_l^A \cdot \vec{e}_p^B dx dy}^{=C_{lp}} = \sum_{p=1}^P \overbrace{T_p \int_0^{b/2} \int_0^{a/2} \vec{e}_l^A \cdot \vec{e}_p^{s,N} dx dy}^{=D_{lp}^{z=dN}} + \sum_{p=1}^P \overbrace{r_p \int_0^{b/2} \int_0^{a/2} \vec{e}_l^A \cdot \vec{e}_p^{s,N} dx dy}^{=D_{lp}^{z=dN}} \tag{3.60}$$

where  $l = 1, 2, 3 \dots P$

$$\sum_{p=1}^P t_p \overbrace{Z_{TM,l}^{s,i} \int_0^{h/2} \int_0^{w/2} \bar{h}_l^s \cdot \bar{h}_p^B dx dy}^{F_{lp}} = \sum_{p=1}^P T_p \overbrace{Z_{TM,l}^{s,i} \int_0^{h/2} \int_0^{w/2} \bar{h}_l^s \cdot \bar{h}_p^{s,N} dx dy}^{P_{lp}} - \sum_{p=1}^P r_p \overbrace{Z_{TM,l}^{s,i} \int_0^{h/2} \int_0^{w/2} \bar{h}_l^s \cdot \bar{h}_p^{s,N} dx dy}^{P_{lp}} \quad (3.61)$$

where  $l = 1, 2, 3 \dots P$

Letting

$$\begin{aligned} U_{lp} &= \left[ A_{11}^p e^{\gamma_p^{s,1} d_1} + A_{21}^p e^{-\gamma_p^{s,1} d_1} \right] D_{lp}^{z=0} \\ V_{lp} &= \left[ A_{12}^p e^{\gamma_p^{s,1} d_1} + A_{22}^p e^{-\gamma_p^{s,1} d_1} \right] D_{lp}^{z=0} \\ W_{lp} &= \left[ A_{11}^p e^{\gamma_p^{s,1} d_1} - A_{21}^p e^{-\gamma_p^{s,1} d_1} \right] Q_{lp} \\ Y_{lp} &= \left[ A_{12}^p e^{\gamma_p^{s,1} d_1} - A_{22}^p e^{-\gamma_p^{s,1} d_1} \right] Q_{lp} \end{aligned}$$

equations (3.58) thru (3.61) can be reduced and re-arranged to become

$$\left. \begin{aligned} \sum_{p=1}^P R_p C_{lp} - \sum_{p=1}^P T_p U_{lp} - \sum_{p=1}^P r_p V_{lp} &= -C_{l1} \\ \sum_{p=1}^P R_p F_{lp} + \sum_{p=1}^P T_p W_{lp} + \sum_{p=1}^P r_p Y_{lp} &= F_{l1} \\ \sum_{p=1}^P T_p D_{lp}^{z=d_N} + \sum_{p=1}^P r_p D_{lp}^{z=d_N} - \sum_{p=1}^P t_p C_{lp} &= 0 \\ \sum_{p=1}^P T_p P_{lp} - \sum_{p=1}^P r_p P_{lp} - \sum_{p=1}^P t_p F_{lp} &= 0 \end{aligned} \right\} \text{where } l = 1, 2, 3 \dots P \quad (3.62)$$

Equation (3.62) can be represented in partitioned-matrix form as

$$\begin{bmatrix} C_{lp} & -U_{lp} & -V_{lp} & 0 \\ F_{lp} & W_{lp} & Y_{lp} & 0 \\ 0 & D_{lp}^{z=d_N} & D_{lp}^{z=d_N} & -C_{lp} \\ 0 & P_{lp} & -P_{lp} & -F_{lp} \end{bmatrix} \begin{bmatrix} R_p \\ T_p \\ r_p \\ t_p \end{bmatrix} = \begin{bmatrix} -C_{l1} \\ F_{l1} \\ 0 \\ 0 \end{bmatrix} \quad (3.63)$$



where  $C_{lp}$ ,  $D_{lp}^{z=d_N}$ ,  $F_{lp}$ ,  $P_{lp}$ ,  $U_{lp}$ ,  $V_{lp}$ ,  $W_{lp}$ , and  $Y_{lp}$  are  $P \times P$  sub-matrices, and  $C_{l1}$  and  $F_{l1}$  are  $P \times 1$  sub-matrices.

Now that the structure of the solution is in place, there remains the arduous task of resolving the eight inner-products  $C_{lp}$ ,  $C_{l1}$ ,  $D_{lp}^{z=0}$ ,  $D_{lp}^{z=d_N}$ ,  $F_{lp}$ ,  $F_{l1}$ ,  $Q_{lp}$ , and  $P_{lp}$ . Because the proofs to these inner-products are lengthy, the respective solutions are provided in Appendix A.

### **3.4 Material Parameter Extraction.**

The first step to extract the test sample's constitutive parameters is to solve (3.63) for the coefficient ratios of (3.48) thru (3.51) via Gaussian elimination. The theoretical solution presented thus far accounts for a finite number of higher-order modes excited at the  $z = 0$  interface, but the only mode that is sensed at both measurement probes is the reflected and transmitted  $TE_{10}$  mode. Even though the higher-order modes exist and significantly affect the complex amplitude of the  $TE_{10}$  mode, they quickly evanesce well in advance of either measurement probe. Having said this, the ratios of interest are  $R_1$  and  $t_1$ , where  $R_1$  and  $t_1$  represent the theoretical reflection and transmission coefficients respectively for the  $TE_{10}$  mode. In terms of theoretical S-parameters,  $R_1 = S_{11}^{thy}(\omega, \varepsilon, \mu)$  and  $t_1 = S_{21}^{thy}(\omega, \varepsilon, \mu)$ . To find  $S_{22}^{thy}$  and  $S_{12}^{thy}$ , the material layers are flipped in order in the software and the material parameter extraction processed repeated.

Now that  $S_{11}^{thy}$ ,  $S_{12}^{thy}$ ,  $S_{21}^{thy}$ , and  $S_{22}^{thy}$  are known for an initial guess at the test sample's constitutive parameters, the next step is to compare them to the measured S-parameters  $S_{11}^{meas}$ ,  $S_{12}^{meas}$ ,  $S_{21}^{meas}$ , and  $S_{22}^{meas}$  according to (3.64).

$$\min \left\{ \sum_i \left[ \left| S_i^{thy}(\omega, \epsilon, \mu) - S_i^{exp}(\omega) \right|^2 \right] \right\} \quad \text{where } i = 11, 21, 22, 12 \quad (3.64)$$

If the difference between the theoretical and measured S-parameters is out of predefined limits, a non-linear least-squares routine is used to adjust the initially guessed constitutive parameters until  $S_{11}^{thy} \approx S_{11}^{meas}$ ,  $S_{12}^{thy} \approx S_{12}^{meas}$ ,  $S_{21}^{thy} \approx S_{21}^{meas}$ , and  $S_{22}^{thy} \approx S_{22}^{meas}$  within the predefined limits. The constitutive parameters used to reach the equivalence are identified as the material's constitutive parameters for the particular frequency. This process is repeated for each measured frequency in an iterative manner until the material's constitutive parameters are calculated across the measured spectrum.

The entire process mentioned in this chapter has been programmed using Matlab<sup>®</sup> Version 7. The application specific function used to solve (3.64) is the non-linear least-squares algorithm (lsqnonlin.m), which is part of Matlab's<sup>®</sup> Optimization Toolbox.

### 3.5 Summary

To adequately account for the higher-order modes excited at the  $z = 0$  interface by the 2-D symmetrically reduced waveguide, modal-analysis was applied and broken up into three distinct tasks. The end result of the three tasks was a partitioned matrix that when solved, provided the theoretical S-parameters for the particular test configuration and initially guessed at test sample constitutive parameters. Once the theoretical S-

parameters were calculated and the experimental S-parameters measured, an optimization routine was applied to the theoretical and measured data yielding the test sample's constitutive parameters for the measured spectrum. The heart of the optimization routine was Matlab's<sup>®</sup> non-linear least-squares root search algorithm.

3. Methodology.....	3-1
3.1 Field Expansions .....	3-2
3.1.1 2-D Stepped-Waveguide Geometry.....	3-2
3.1.2 Derivation of Higher-Order Scattered Fields.....	3-4
3.1.3 Mode Orthogonality.....	3-8
3.1.4 Field Expansions in Waveguide Regions.....	3-10
3.1.5 Field Expansions in Sample Region.....	3-13
3.2 Satisfying Boundary Conditions .....	3-15
3.3 Testing with Integral Operators .....	3-19
3.4 Material Parameter Extraction.....	3-23
3.5 Summary .....	3-24

**Figure 3-1** Cross-sectional view of 2-D stepped waveguide fixture looking at the  $z = 0$  interface. Symbols  $\vec{J}_s$  identify excited surface currents caused by the incident  $TE_{10}$  wave..... 3-3

**Figure 3-2** Top view of 2-D reduced aperture waveguide fixture having one unknown layer (i.e. center) and multiple known layers. This arrangement presents a generic view that encompasses all possible sample holder configurations. Sample holder width exaggerated to adequately detail sample region. Symbols  $\vec{J}_s$  identify excited surface currents caused by incident  $TE_{10}$  wave..... 3-3

**Figure 3-3** Side view of 2-D reduced aperture waveguide fixture having one unknown layer (i.e. center) and multiple known layers..... 3-4

#### ***4. Results and Error Analysis***

In order to validate the reduced aperture modal analysis solution discussed in previous chapters, an S-band (approximately 2.6 – 3.95 GHz ) waveguide fitted with custom designed, reduced aperture sample holders was used as a proof-of-concept demonstration. Because the solution developed in this effort targets low-frequency applications using much larger waveguides, the user-friendly, Graphical User Interface (GUI) based, Matlab<sup>®</sup> program developed to process the experimental measured data can be easily modified to accommodate any rectangular waveguide geometry and varying (both 1-D and 2-D) reduced apertures.

For the test configuration, sample holders that reduce the S-band waveguide's cross-sectional area by 25%, 50%, and 75% were used. Test samples consisted of acrylic and magnetic radar absorbing material (MRAM). The reduced aperture results will be compared to the full-aperture data to verify the solution's accuracy. Furthermore, reduced aperture results will be computed and plotted using an increasing number of higher-order modes to demonstrate convergence to the known, full-aperture, material parameters.

As every experimental measurement process includes a certain degree of error, an error analysis of the measured data was performed. The greatest contributors of uncertainty in this particular measurement process were determined to be reduced aperture dimensions (height and/or width), sample placement, and S-parameters measured by the HP8510B Network Analyzer. The respective error bounds were included in the processed results.

#### ***4.1 Reduced Aperture Experimental Setup***

The reduced aperture experimental setup is as shown in Figure 4-1 with the WR284 (S-band) waveguide connected to a HP8510B via coaxial cables. The reduced aperture sample holders were aligned with the S-band waveguide using precision alignment pins to correctly align the waveguide's walls to the aperture's walls. Each sample holder had S-band through-hole bolt patterns to facilitate mating the S-band waveguide to the sample holder.

The three sample holders used to validate the reduced aperture modal-analysis technique are shown in Figure 4-2. The left-most sample holder has dimensions of 2.46"×1.16" and reduces the S-band feed waveguide cross-sectional area by 25%. The middle sample holder has dimensions of 2.01"×.95" and reduces the S-band waveguide cross-sectional area by 50%. Finally, the right-most sample holder has dimensions of 1.42"×.67" and reduces the S-band waveguide cross-sectional area by 75%.

Before any reduced aperture measurements were taken, a full 2-port thru, reflect, line (TRL) calibration was performed to establish the measurement planes at  $z = 0$  and  $z = d_N$  (see Figures 3-2 and 3-3).



**Figure 4-1.** Experimental setup showing the WR284 waveguide connected to an HP8510B Network Analyzer via coaxial cables. The reduced-aperture sample holder is mounted between the waveguide feeds using precision alignment pins.

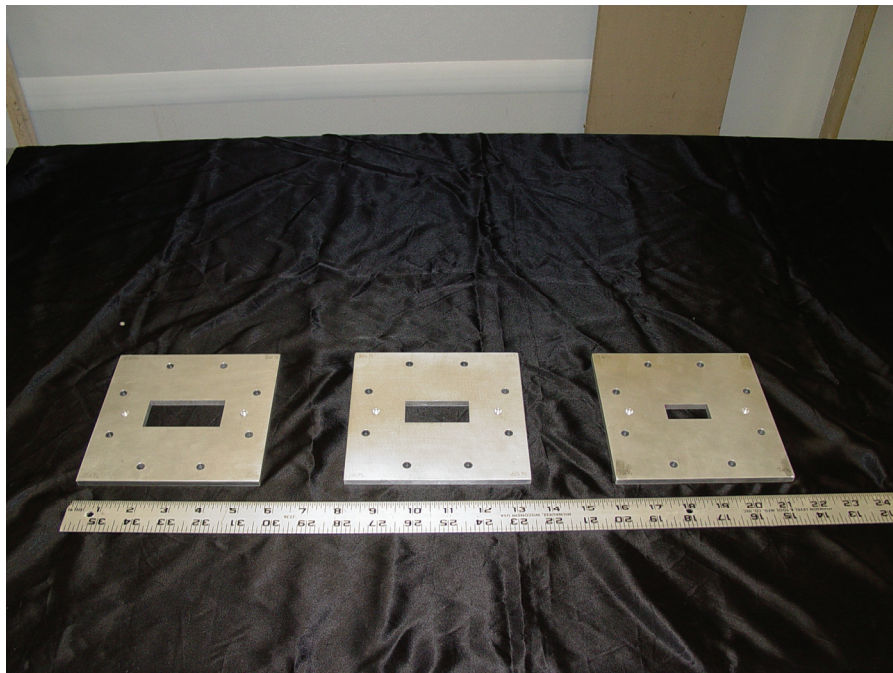


**Figure 4-2** S-band reduced aperture sample holders. From left to right are: 25% (2.46"×1.16") reduced waveguide sample holder, 50% (2.01"×.95") reduced waveguide sample holder and the 75% (1.42"×.67") reduced waveguide sample holder.

## 4.2 Error Analysis

To adequately account for the test sample dimensions and placement measurement errors, a differential error analysis was performed similar to the 1-D waveguide reduction effort [10] and is provided for the interested reader. With the estimated permittivity written as a function of thickness  $\ell$  and placement  $p$ ,

$$\varepsilon = \varepsilon'(\ell, p) - j\varepsilon''(\ell, p) \quad (4.1)$$

the Taylor series expansion of the real part around the point  $(\ell_o, p_o)$  is given as

$$\varepsilon'(\ell_o + \Delta\ell, p_o + \Delta p) = \varepsilon'(\ell_o, p_o) + \frac{\partial\varepsilon'(\ell_o, p_o)}{\partial\ell}\Delta\ell + \frac{\partial\varepsilon'(\ell_o, p_o)}{\partial p}\Delta p + \dots \quad (4.2)$$

where  $\Delta\ell$  is the uncertainty in the measured thickness  $\ell_o$ , and  $\Delta p$  is the uncertainty in placement at the location  $p_o$ . For relatively small  $\Delta\ell$  and  $\Delta p$ , the higher-order terms of the Taylor series expansion can be neglected and the change in the real permittivity can be represented as

$$\Delta\varepsilon'_{exact} = \varepsilon'(\ell_o + \Delta\ell, p_o + \Delta p) - \varepsilon'(\ell_o, p_o) \approx \frac{\partial\varepsilon'(\ell_o, p_o)}{\partial\ell}\Delta\ell + \frac{\partial\varepsilon'(\ell_o, p_o)}{\partial p}\Delta p = \Delta\varepsilon'_{approx} \quad (4.3)$$

Next, the partial derivatives can be approximated (again assuming small  $\Delta\ell$  and  $\Delta p$ ) by

$$\Delta\varepsilon'_\ell = \frac{\partial\varepsilon'(\ell_o, p_o)}{\partial\ell}\Delta\ell \approx \frac{\varepsilon'(\ell_o + \Delta\ell, p_o) - \varepsilon'(\ell_o, p_o)}{\Delta\ell}\Delta\ell = \varepsilon'(\ell_o + \Delta\ell, p_o) - \varepsilon'(\ell_o, p_o) \quad (4.4)$$

$$\Delta\varepsilon'_p = \frac{\partial\varepsilon'(\ell_o, p_o)}{\partial p}\Delta p \approx \frac{\varepsilon'(\ell_o, p_o + \Delta p) - \varepsilon'(\ell_o, p_o)}{\Delta p}\Delta p = \varepsilon'(\ell_o, p_o + \Delta p) - \varepsilon'(\ell_o, p_o) \quad (4.5)$$

In general,  $\Delta\ell$  and  $\Delta p$  can be positive or negative values. For small relative perturbations, the respective errors  $\Delta\varepsilon'_\ell$  and  $\Delta\varepsilon'_p$  will be symmetric about the



unperturbed  $\varepsilon'(\ell_o, p_o)$ . However, for larger perturbations, the symmetry will start to break down and the errors generated by the positive and negative values must be computed separately to determine the worst-case contributions.

It should also be clear that independent material parameter extractions for the perturbations in the measured thickness and placement of the test sample can be conducted and then combined to determine the overall error bounds related to those specific uncertainties. In combining the results, the triangle inequality is used to form an approximation of the worst-case errors in the real permittivity

$$|\Delta\varepsilon'_{approx}| = |\Delta\varepsilon'| = |\Delta\varepsilon'_\ell + \Delta\varepsilon'_p| \leq |\Delta\varepsilon'_\ell| + |\Delta\varepsilon'_p| \quad (4.6)$$

The triangle inequality is generally applied to vectors with the geometric interpretation that the sum of the lengths of any two sides of a triangle is always greater than the length of the remaining side. In this case, where  $\Delta\varepsilon'_\ell, \Delta\varepsilon'_p$  are scalar quantities, the inequality is simply used to prevent cancellation between positive and negative error contributions.

It must be noted that often independent error contributions are added in quadrature [4] (i.e.,  $|\Delta\varepsilon'| = \sqrt{(\Delta\varepsilon'_\ell)^2 + (\Delta\varepsilon'_p)^2}$ ), but that assumes normally distributed errors where the sum of all deviations around the nominally measured values are negligible. In addition, the least-squares optimization algorithm tends to further exacerbate the problem, thus favoring the worst-case approach. Finally, the error analyses for the imaginary permittivity and real and imaginary permeability follow in a similar manner. The third source of error accounted for in this error analysis was the uncertainty associated with the HP8510B Network analyzer. The associated error values

relating to this type of measurement were provided in the analyzer's documentation and used in the error analysis.

### ***4.3 Reduced Aperture Results for Acrylic Test Sample***

The acrylic samples characterized during this were a clear plexiglass-type material that exhibited almost pure dielectric characteristics with very little loss and no magnetic properties as observed when tested using the full-aperture method. In fact, the results from the full aperture measurements taken with this material closely matched documented [7] constitutive parameters for polystyrene.

A key benefit to using acrylic apart from its well-documented constitutive parameters is the fact that it is easy to machine due to its rigid properties. The acrylic samples used in all measurements were machined to superior precision providing a very tight fit when inserted into the respective sample holder's aperture. This feature minimized error induced from gaps. For the reduced aperture measurements, the acrylic samples were machined to match the sample holder's uniform thickness (.254 in.) exactly.

The first measurement was conducted using the 25% reduction sample holder. This sample holder minimized the feeding S-band waveguide cross-sectional dimensions from 2.84"×1.34" to 2.46"×1.16" realizing a 25% cross-sectional area reduction. Because the test samples were machined to match the sample holder's uniform thickness (.254 in.), the test sample was mounted flush on both sides with respect to the sample holder. From an error analysis perspective, this attribute was attractive because it reduced the placement uncertainty to zero. Figure 4-3 shows that approximately 20

modes were required to converge to the full-aperture solution. This implies that the energy distributed into the higher-order modes must be accounted for to accurately characterize the material.

The second measurement was conducted using the 50% reduction sample holder. This sample holder minimized the feeding S-band waveguide cross-sectional dimensions from 2.84"×1.34" to 2.01"×.95" realizing a 50% cross-sectional area reduction. Figure 4-4 shows that approximately 20 modes were required to converge to the full-aperture solution.

The third and last acrylic measurement used the 75% reduction sample holder. This sample holder minimized the feeding S-band waveguide cross-sectional dimensions from 2.84"×1.34" to 1.42"×.67" realizing a 75% cross-sectional area reduction. By inspecting Figure 4-5, it is evident that the modal-analysis solution was unable to converge to the full-aperture results and displayed an approximate 11% degree of error. This error was caused by the 75% reduced aperture acting like a filter at the higher frequencies such that all of the energy launched into region A effectively transmitted through the aperture leaving very little energy to be reflected back to the launcher probe. From an S-parameter perspective,  $S_{12}$  and  $S_{21}$  approached unity, whereas  $S_{11}$  and  $S_{22}$  approached zero at the higher end of the S-band spectrum.

As mentioned earlier, the acrylic test material demonstrated little to no electric loss or magnetic properties during the full-aperture material characterization. With this in mind, the permittivity imaginary component and complex permeability were not provided in this section as they were not considered value-added.

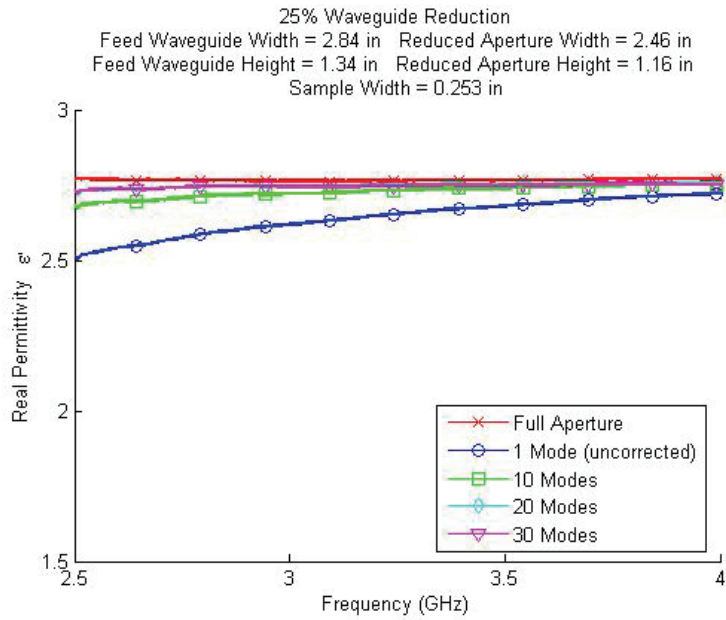


**Figure 4-3.** Real permittivity for acrylic test sample mounted in the 2.46"×1.16", 25% reduction sample holder. Approximately 20 modes are required for convergence to the full-aperture baseline.

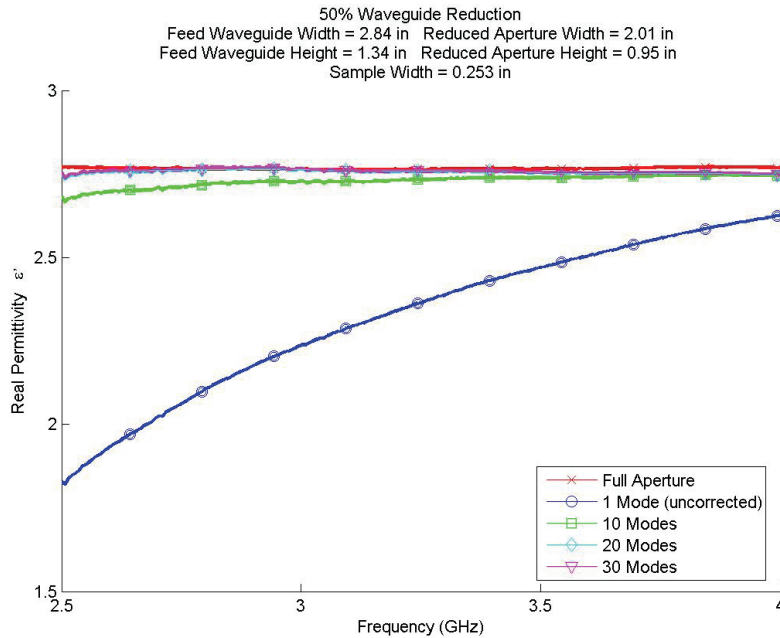


**Figure 4-4.** Real permittivity for acrylic test sample mounted in the 2.01"×.95", 50% reduction sample holder. Approximately 20 modes are required for convergence to the full-aperture baseline.

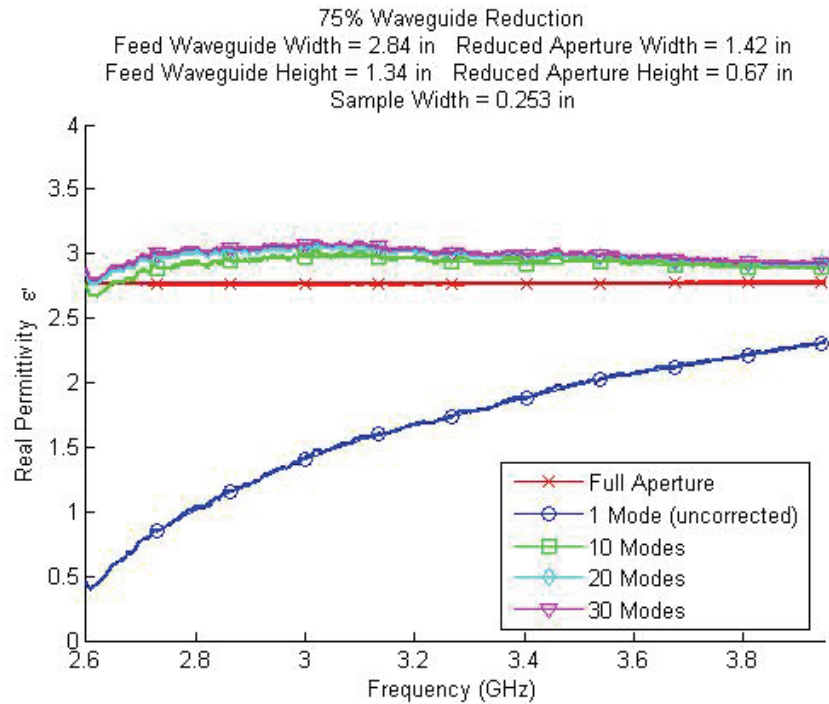


**Figure 4-5.** Real permittivity for acrylic test sample mounted in the 1.42"×.67" , 75% reduction sample holder. Approximate 11% error caused by uncorrectable scratches and blemishes on sample's surface.

#### 4.4 Reduced Aperture Results for MRAM Test Sample

In order to subject the reduced aperture modal-analysis solution to a more realistic scenario, a MRAM test sample was chosen that is considerably more complex and lossy than acrylic. The same steps that were used to electromagnetically characterize acrylic in the 25%, 50%, and 75% reduction sample holders were used to test the MRAM sample. Unlike the acrylic test sample placement where the sample was flush on both sides of the sample holder, the thinner MRAM test samples were flush on only the front side ( $z = 0^+$ ) of the sample holder. The remainder of the sample holder was vacant of material, leaving free-space as the filling medium.

The results for the MRAM characterized in the 25% reduced aperture sample holder are compared to the full-aperture data in Figures 4-6 and 4-7. The permittivity deviated from the ideal full-aperture permittivity because the sample's inability to maintain a rigid planar posture within the sample holder. This non-planar posture also created gaps between the sample holder and sample material. Because the sample holder's width (.253 in.) was so thin, it could not accommodate sample support structures. The full-aperture measurements were conducted using known materials as supporting structures on both sides of the test sample as the full-aperture sample holder width (1.2 in.) could handle multiple structures. The error in permeability was also a result of the sample's inability to maintain a rigid planar posture within the sample holder.

Figures 4-8 and 4-9 show the results for the MRAM characterized in the 50% reduced aperture sample holder and compares the data to the full-aperture results. Similar to the 25% waveguide reduction results, both the permittivity and permeability experienced an error caused by the sample's non-planar posture and subsequent gaps within the sample holder.

Figures 4-10 and 4-11 show the results for the MRAM characterized in the 75% reduced aperture sample holder and compares the data to the full-aperture results. Again, error was introduced by the non-planar posture and gaps within the sample holder. Similar to the 75% acrylic measurements, the minimal energy reflected back into region A approached the noise floor causing additional error.

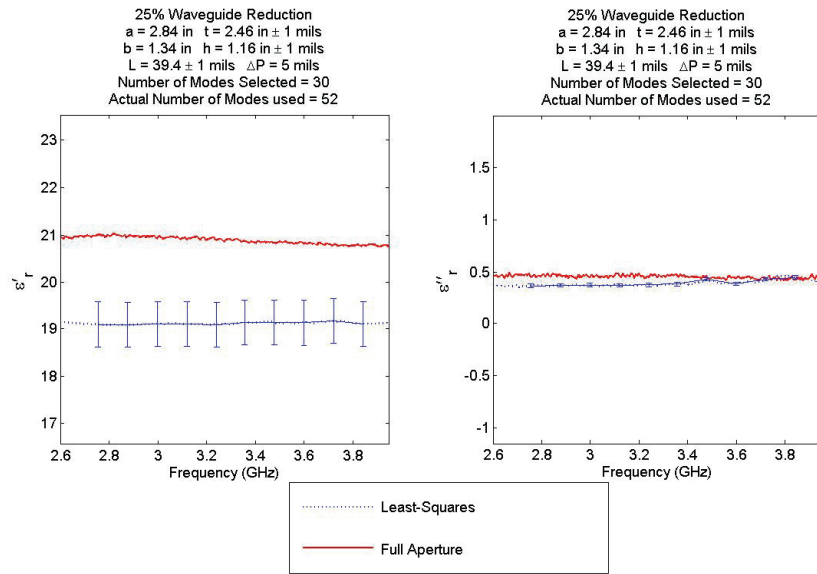


**Figure 4-6.** Permittivity of MRAM test sample mounted in 2.46"×1.16", 25% reduction sample holder.

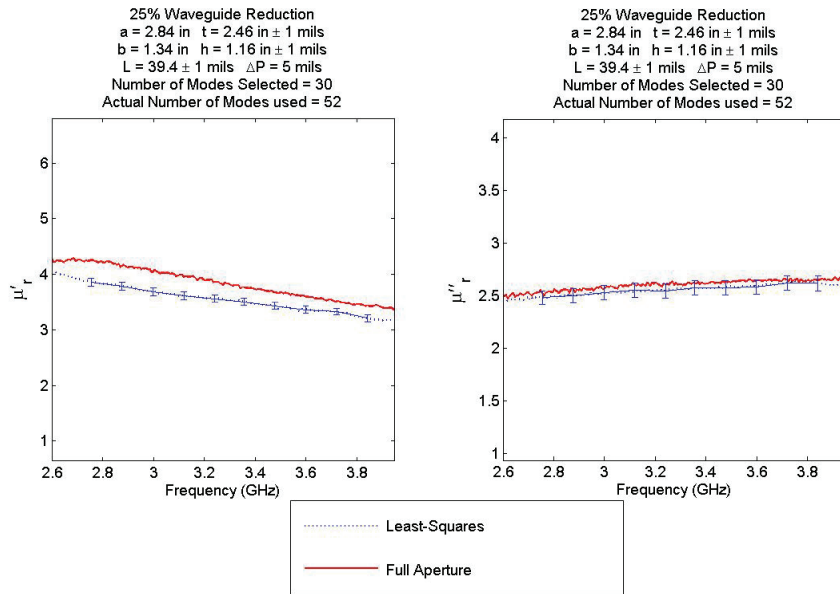


**Figure 4-7.** Permeability of MRAM test sample mounted in 2.46"×1.16", 25% reduction sample holder.

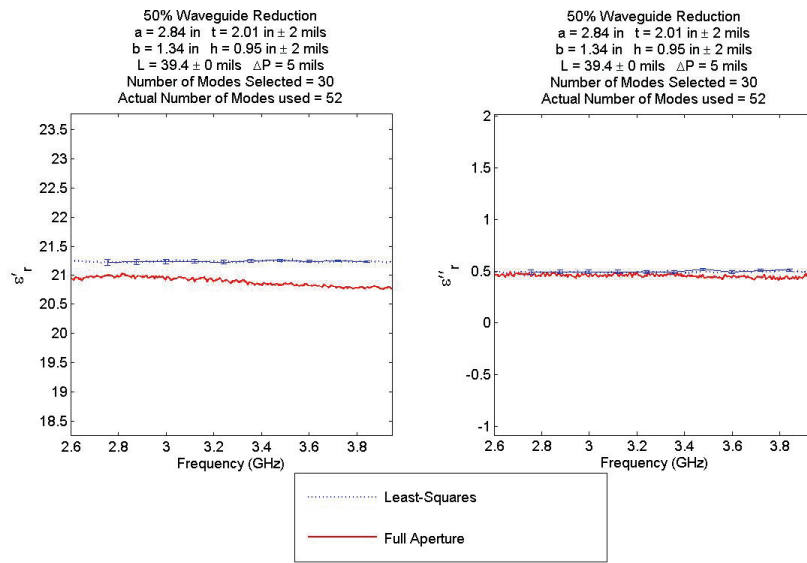


**Figure 4-8.** Permittivity of MRAM test sample mounted in the 2.01"×.95" , 50% reduction sample holder.

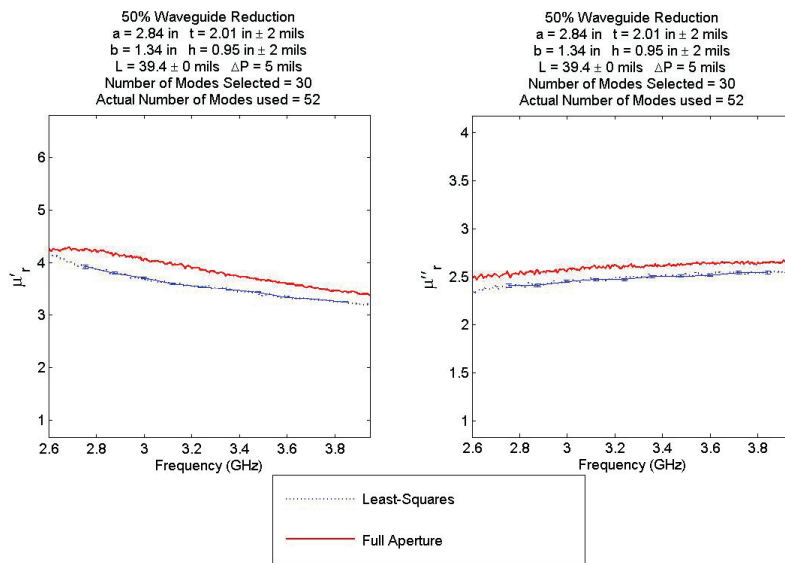


**Figure 4-9.** Permeability of MRAM test sample mounted in the 2.01"×.95" , 50% reduction sample holder.



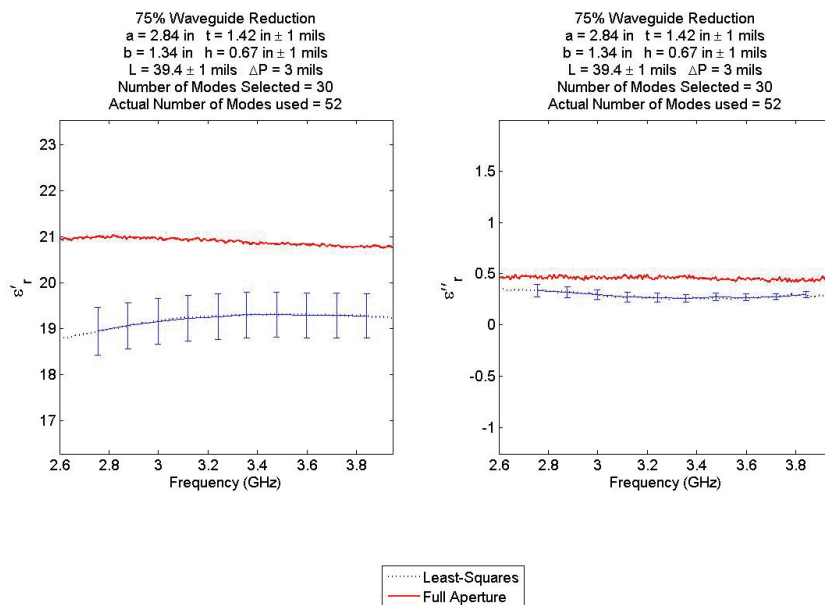


**Figure 4-10** Permittivity of MRAM test sample mounted in the 1.42"×.67" , 75% reduction sample holder.

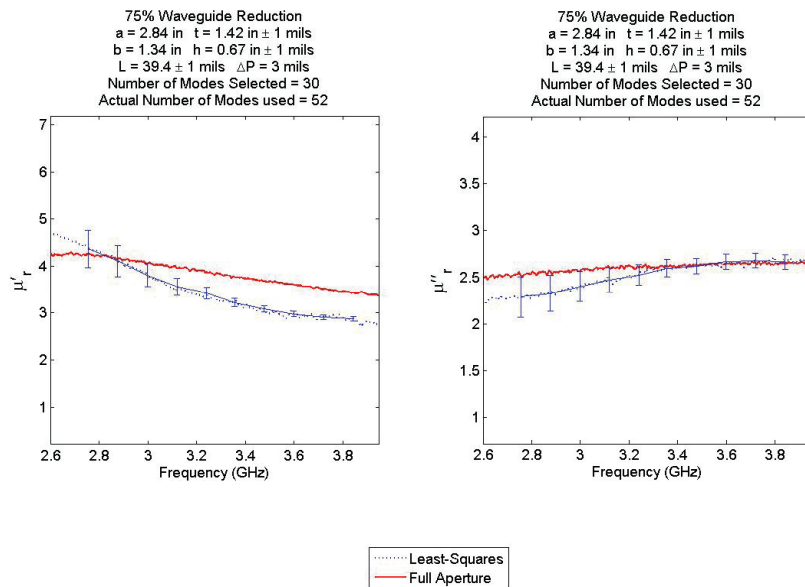


**Figure 4-11** Permeability of MRAM test sample mounted in the 1.42"×.67" , 75% reduction sample holder.

#### ***4.5 Summary***

Acrylic and MRAM test samples mounted in 2-D reduced-width S-band sample holders were used to verify the modal analysis technique. The acrylic results were excellent, but there was a certain degree of error associated with the MRAM measurements caused by the sample's inability to maintain a rigid planar posture within the sample holder and related gaps. The 75% reduction measurements were found to be degraded as the minimal energy transmitted into Region B approached the noise floor of the Network Analyzer, thus corrupting the  $S_{21}$  measured data.

It was shown that the number of higher-order modes required for convergence is directly related to the degree of width reduction to the sample holder. Finally, a differential error analysis was presented to form error bounds related to human errors in measurement of test sample thickness and placement.

4. Results and Error Analysis .....	4-1
4.1 Reduced Aperture Experimental Setup.....	4-2
4.2 Error Analysis .....	4-4
4.3 Reduced Aperture Results for Acrylic Test Sample .....	4-6
4.4 Reduced Aperture Results for MRAM Test Sample.....	4-9
4.5 Summary .....	4-14

<b>Figure 4-1.</b> Experimental setup showing the WR284 waveguide connected to an HP8510B Network Analyzer via coaxial cables. The reduced-aperture sample holder is mounted between the waveguide feeds using precision alignment pins. ....	4-3
<b>Figure 4-2</b> S-band reduced aperture sample holders. From left to right are: 25% (2.46"×1.16") reduced waveguide sample holder, 50% (2.01"×.95") reduced waveguide sample holder and the 75% (1.42"×.67") reduced waveguide sample holder. ....	4-3
<b>Figure 4-3.</b> Real permittivity for acrylic test sample mounted in the 2.46"×1.16", 25% reduction sample holder. Approximately 20 modes are required for convergence to the full-aperture baseline. ....	4-8
<b>Figure 4-4.</b> Real permittivity for acrylic test sample mounted in the 2.01"×.95", 50% reduction sample holder. Approximately 20 modes are required for convergence to the full-aperture baseline. ....	4-8
<b>Figure 4-5.</b> Real permittivity for acrylic test sample mounted in the 1.42"×.67", 75% reduction sample holder. Approximate 11% error caused by uncorrectable scratches and blemishes on sample's surface. ....	4-9
<b>Figure 4-6.</b> Permittivity of MRAM test sample mounted in 2.46"×1.16", 25% reduction sample holder.....	4-11
<b>Figure 4-7.</b> Permeability of MRAM test sample mounted in 2.46"×1.16", 25% reduction sample holder.....	4-11
<b>Figure 4-8.</b> Permittivity of MRAM test sample mounted in the 2.01"×.95", 50% reduction sample holder.....	4-12
<b>Figure 4-9.</b> Permeability of MRAM test sample mounted in the 2.01"×.95", 50% reduction sample holder.....	4-12
<b>Figure 4-10</b> Permittivity of MRAM test sample mounted in the 2.01"×.95", 75% reduction sample holder.....	4-13

**Figure 4-11** Permeability of MRAM test sample mounted in the 2.01"×.95" , 75%  
reduction sample holder..... 4-13

## ***5. Conclusion and Recommendations***

A 2-D stepped-waveguide technique was developed to extract permittivity and permeability of smaller test samples mounted in a larger rectangular waveguide measurement system. A mode-matching technique was implemented that accounted for higher-order transverse electric and transverse magnetic modes excited by the discontinuity at the reduced aperture. The sample permittivity and permeability were iteratively solved via a MatLab-based nonlinear least-squares algorithm used to compare the theoretical S-parameters from the modal analysis solution to the actual measured S-parameters obtained from the HP8510B Network Analyzer.

The reduced-aperture material characterization technique was experimentally verified for non-magnetic materials through comparisons of 25% and 50% reduced waveguide measurements of acrylic to full-aperture acrylic measurements. MRAM was used to verify the modal analysis solution could simultaneously extract both permittivity and permeability of magnetic materials. Comparing reduced aperture measurements to full-aperture measurements validated the modal-analysis solution for both non-magnetic and magnetic materials. The comparisons also indicated that approximately 20 higher-order modes were required to converge to the full-aperture results.

A differential error analysis conducted on test sample thickness and placement uncertainties explained most of the discrepancies from the full-aperture baselines noted during the MRAM testing.

## ***5.1 Future Research***

In contrast to the problems associated with low-frequency material characterization, high-frequency material characterization is not without its own set of constraints. For example, measuring a material's constitutive parameters in the S-band demands that the sample size be cut to standard S-band waveguide (WR284) cross-sectional dimensions (2.84 inches by 1.34 inches). Similarly, measuring a material's constitutive parameters in the X-band requires the sample size be cut to standard X-band waveguide (WR90) cross-sectional dimensions (.9 inches by .4 inches). As the tested band increases in frequency, the sample's dimensions are further reduced.

A solution to this problem would be to use a single test sample to measure multiple high-frequency radar bands via a waveguide expansion configuration. A modal analysis solution similar to the method developed in this effort could be used to accommodate the higher-order modes within the various waveguide regions.

5. Conclusion and Recommendations.....	5-1
5.1 Future Research.....	5-2

## Appendix A Proofs of Inner-Products

### A.1 Proof for $C_{lp}$

For the inner-product represented by  $C_{lp}$ , there are four possible combinations of inner-products (i.e.  $TE \bullet TE$ ,  $TE \bullet TM$ ,  $TM \bullet TE$ , and  $TM \bullet TM$ ). If both  $\vec{e}_l^A$  and  $\vec{e}_p^A$  are  $TE$ , the inner-product results in

$$C_{lp}^{TE \bullet TE} = \int_0^{b/2} \int_0^{a/2} \vec{e}_l^A \cdot \vec{e}_p^A dx dy = \begin{cases} \frac{ab}{8} (k_{c,p}^A)^2 & \dots \text{if } l = p \text{ and } n = 0 \\ \frac{ab}{16} (k_{c,p}^A)^2 & \dots \text{if } l = p \text{ and } n \neq 0 \\ 0 & \dots \text{if } l \neq p \end{cases} \quad (\text{A.1})$$

If  $\vec{e}_l^A$   $TE$  and  $\vec{e}_p^A$   $TM$ , the inner-product results in

$$C_{lp}^{TE \bullet TM} = \int_0^{b/2} \int_0^{a/2} \vec{e}_l^A \cdot \vec{e}_p^A dx dy = 0 \quad (\text{A.2})$$

If  $\vec{e}_l^A$   $TM$  and  $\vec{e}_p^A$   $TE$ , the inner-product results in

$$C_{lp}^{TM \bullet TE} = \int_0^{b/2} \int_0^{a/2} \vec{e}_l^A \cdot \vec{e}_p^A dx dy = 0 \quad (\text{A.3})$$

And, if both  $\vec{e}_l^A$  and  $\vec{e}_p^A$  are  $TM$ , the inner-product results in

$$C_{lp}^{TM \bullet TM} = \int_0^{b/2} \int_0^{a/2} \vec{e}_l^A \cdot \vec{e}_p^A dx dy = \begin{cases} \frac{ab}{16} (k_{c,p}^A)^2 & \dots \text{if } l = p \\ 0 & \dots \text{if } l \neq p \end{cases} \quad (\text{A.4})$$

Therefore,  $C_{lp}$  will always be a  $P \times P$  matrix with non-diagonal elements equal to zero, and the diagonal elements equal to the results from either (A.1) or (A.4).



### A.2 Proof for $C_{ll}$

For the inner-product represented by  $C_{ll}$ , there are only two possible combinations of inner-products as  $p=l$  for all cases. Because  $\vec{e}_p^A$  is restricted to  $\vec{e}_1^A$ , the inner product combinations are either  $TE \bullet TE_{10}$  or  $TM \bullet TE_{10}$ . If  $\vec{e}_l^A$  is  $TE$ , the inner-product  $C_{ll}$  results in

$$C_{ll}^{TE \bullet TE_{10}} = \int_0^{b/2} \int_0^{a/2} \vec{e}_l^A \cdot \vec{e}_1^A dx dy = \begin{cases} \frac{ab}{8} (k_{c,1}^A)^2 & \dots \text{if } l = p = 1 \\ 0 & \dots \text{if } l \neq p \end{cases} \quad (\text{A.5})$$

And, if  $\vec{e}_l^A$  is  $TM$ , the inner-product  $C_{ll}$  results in

$$C_{ll}^{TM \bullet TE_{10}} = \int_0^{b/2} \int_0^{a/2} \vec{e}_l^A \cdot \vec{e}_1^A dx dy = 0 \quad (\text{A.6})$$

Therefore, matrix  $C_{ll}$  will be  $P \times l$  in form with only the first element being equal to (A.5). All other elements besides the first element will be equal to zero. It is important to note that  $C_{ll}$  is merely the first column from matrix  $C_{lp}$ .

### A.3 Proof for $Q_{lp}$

For the inner-product represented by  $Q_{lp}$ , there are also four possible combinations of inner-products. If both  $\vec{h}_l^s$  and  $\vec{h}_p^{s,1}$  are  $TE$ , the inner-product becomes

$$Q_{lp}^{TE \bullet TE} = Z_{TM,l}^{s,i} \int_0^{h/2} \int_0^{w/2} \vec{h}_l^s \cdot \vec{h}_p^{s,1} dx dy = \begin{cases} \frac{hw}{8 \bullet Z_{TE,p}^{s,1}} (k_{c,p}^s)^2 & \dots \text{if } l = p \text{ and } n = 0 \\ \frac{hw}{16 \bullet Z_{TE,p}^{s,1}} (k_{c,p}^s)^2 & \dots \text{if } l = p \text{ and } n \neq 0 \\ 0 & \dots l \neq p \end{cases} \quad (\text{A.7})$$

If  $\vec{h}_l^s$  *TE* and  $\vec{h}_p^{s,1}$  *TM*, inner-product  $Q_{lp}$  becomes

$$Q_{lp}^{TE \bullet TM} = Z_{TM,l}^{s,i} \int_0^{h/2} \int_0^{w/2} \vec{h}_l^s \cdot \vec{h}_p^{s,1} dx dy = 0 \quad (\text{A.8})$$

If  $\vec{h}_l^s$  *TM* and  $\vec{h}_p^{s,1}$  *TE*, inner-product  $Q_{lp}$  becomes

$$Q_{lp}^{TM \bullet TE} = Z_{TM,l}^{s,i} \int_0^{h/2} \int_0^{w/2} \vec{h}_l^s \cdot \vec{h}_p^{s,1} dx dy = 0 \quad (\text{A.9})$$

Finally, if both  $\vec{h}_l^s$  and  $\vec{h}_p^{s,1}$  are *TM*, inner-product  $Q_{lp}$  becomes

$$Q_{lp}^{TM \bullet TM} = Z_{TM,l}^{s,i} \int_0^{h/2} \int_0^{w/2} \vec{h}_l^s \cdot \vec{h}_p^{s,1} dx dy = \begin{cases} \frac{hw}{16 \bullet Z_{TM,p}^{s,1}} (k_{c,p}^s)^2 & \dots l = p \\ 0 & \dots l \neq p \end{cases} \quad (\text{A.10})$$

Similar to  $C_{lp}$ ,  $Q_{lp}$  will also be a  $P \times P$  matrix with all non-diagonal elements equal to zero, and diagonal elements equal to the results from (A.7) or (A.10).

#### A.4 Proof for $P_{lp}$

Inner-product  $P_{lp}$  has a solution almost identical to inner-product  $Q_{lp}$  with the only differences being terms  $\varepsilon_1$  and  $\gamma_p^{s,1}$ . Therefore, if both  $\vec{h}_l^s$  and  $\vec{h}_p^{s,N}$  are  $TE$ , the inner-product becomes

$$P_{lp}^{TE \bullet TE} = Z_{TM,l}^{s,i} \int_0^{h/2} \int_0^{w/2} \vec{h}_l^s \cdot \vec{h}_p^{s,N} dx dy = \begin{cases} \frac{hw}{8 \bullet Z_{TE,p}^{s,N}} (k_{c,p}^S)^2 & \dots \text{if } l = p \text{ and } n = 0 \\ \frac{hw}{16 \bullet Z_{TE,p}^{s,N}} (k_{c,p}^S)^2 & \dots \text{if } l = p \text{ and } n \neq 0 \\ 0 & \dots l \neq p \end{cases} \quad (\text{A.11})$$

If  $\vec{h}_l^s$   $TE$  and  $\vec{h}_p^{s,N}$   $TM$ , inner-product  $P_{lp}$  becomes

$$P_{lp}^{TE \bullet TM} = Z_{TM,l}^{s,i} \int_0^{h/2} \int_0^{w/2} \vec{h}_l^s \cdot \vec{h}_p^{s,N} dx dy = 0 \quad (\text{A.12})$$

If  $\vec{h}_l^s$   $TM$  and  $\vec{h}_p^{s,N}$   $TE$ , inner-product  $P_{lp}$  becomes

$$P_{lp}^{TM \bullet TE} = Z_{TM,l}^{s,i} \int_0^{h/2} \int_0^{w/2} \vec{h}_l^s \cdot \vec{h}_p^{s,N} dx dy = 0 \quad (\text{A.13})$$

Finally, if both  $\vec{h}_l^s$  and  $\vec{h}_p^{s,N}$  are  $TM$ , inner-product  $P_{lp}$  becomes

$$P_{lp}^{TM \bullet TM} = Z_{TM,l}^{s,i} \int_0^{h/2} \int_0^{w/2} \vec{h}_l^s \cdot \vec{h}_p^{s,N} dx dy = \begin{cases} \frac{hw}{16 \bullet Z_{TM,p}^{s,N}} (k_{c,p}^S)^2 & \dots \text{if } l = p \\ 0 & \dots l \neq p \end{cases} \quad (\text{A.14})$$

### A.5 Proof for $D_{lp}$

For  $D_{lp}$ , there are also four possible combinations of inner-products. Before the results are provided for the four mode combinations, there are a few identities derived to make the answers more manageable. Therefore, let

$$A_1 = \int_0^{t/2} \sin(k_{x,m}^A x) \sin(k_{x,m}^S x) dx = \begin{cases} \frac{t}{4} & \dots \text{for } k_{x,m}^A = k_{x,m}^S \\ \frac{\sin\left[\left(k_{x,m}^A - k_{x,m}^S\right)\frac{t}{2}\right]}{2\left(k_{x,m}^A - k_{x,m}^S\right)} - \frac{\sin\left[\left(k_{x,m}^A + k_{x,m}^S\right)\frac{t}{2}\right]}{2\left(k_{x,m}^A + k_{x,m}^S\right)} & \dots \text{for } k_{x,m}^A \neq k_{x,m}^S \end{cases}$$

$$A_2 = \int_0^{h/2} \sin(k_{y,n}^A y) \sin(k_{y,n}^S y) dy = \begin{cases} 0 & \dots k_{y,n}^A = 0, \text{ or } k_{y,n}^S = 0 \\ \frac{h}{4} & \dots k_{y,n}^A = k_{y,n}^S \neq 0 \\ \frac{\sin\left[\left(k_{y,n}^A - k_{y,n}^S\right)\frac{h}{2}\right]}{2\left(k_{y,n}^A - k_{y,n}^S\right)} - \frac{\sin\left[\left(k_{y,n}^A + k_{y,n}^S\right)\frac{h}{2}\right]}{2\left(k_{y,n}^A + k_{y,n}^S\right)} & \dots k_{y,n}^A \neq k_{y,n}^S \end{cases}$$

$$B_1 = \int_0^{t/2} \cos(k_{x,m}^A x) \cos(k_{x,m}^S x) dx = \begin{cases} \frac{t}{4} & \dots \text{for } k_{x,m}^A = k_{x,m}^S \\ \frac{\sin\left[\left(k_{x,m}^A - k_{x,m}^S\right)\frac{t}{2}\right]}{2\left(k_{x,m}^A - k_{x,m}^S\right)} + \frac{\sin\left[\left(k_{x,m}^A + k_{x,m}^S\right)\frac{t}{2}\right]}{2\left(k_{x,m}^A + k_{x,m}^S\right)} & \dots \text{for } k_{x,m}^A \neq k_{x,m}^S \end{cases}$$

$$B_2 = \int_0^{h/2} \cos(k_{y,n'}^A y) \cos(k_{y,n}^S y) dy = \begin{cases} 0 & \dots k_{y,n'}^A = 0 \\ \frac{h}{4} & \dots k_{y,n'}^A = k_{y,n}^S \neq 0 \\ \frac{h}{2} & \dots k_{y,n'}^A = k_{y,n}^S = 0 \\ \frac{\sin \left[ (k_{y,n'}^A - k_{y,n}^S) \frac{h}{2} \right]}{2(k_{y,n'}^A - k_{y,n}^S)} + \frac{\sin \left[ (k_{y,n'}^A + k_{y,n}^S) \frac{h}{2} \right]}{2(k_{y,n'}^A + k_{y,n}^S)} & \dots \text{otherwise} \end{cases}$$

Although the identities provided are constructed for the *TE-TE* case, they are compatible to the *TE-TM*, *TM-TE*, and *TM-TM* cases. For example  $k_{y,n'}^A$  is interchangeable with  $k_{y,s'}^A$ ,  $k_{y,n}^S$  is interchangeable with  $k_{y,s}^S$ ,  $k_{x,m'}^A$  is interchangeable with  $k_{x,r'}^A$ , and  $k_{x,m}^S$  is interchangeable with  $k_{x,r}^S$ . If both  $\vec{e}_l^A$  and  $\vec{e}_p^{s,1}$  are *TE*, the inner-product  $D_{lp}^{z=0}$  results in

$$D_{lp}^{z=0, TE \bullet TE} = \int_0^{b/2} \int_0^{a/2} \vec{e}_l^A \cdot \vec{e}_p^{s,1} dx dy = k_{y,n}^A k_{y,n}^S (A_1 \bullet A_2) + k_{x,m}^A k_{x,m}^S (B_1 \bullet B_2) \quad (\text{A.15})$$

where  $\gamma_p^{s,1}$  and  $\mu_1$  are the propagation constant and permeability of the first layer (see Figure 3.2).

If  $\vec{e}_l^A$  *TE* and  $\vec{e}_p^{s,1}$  *TM*, inner-product  $D_{lp}^{z=0}$  results in

$$D_{lp}^{z=0, TE \bullet TM} = \int_0^{b/2} \int_0^{a/2} \vec{e}_l^A \cdot \vec{e}_p^{s,1} dx dy = k_{y,n}^A k_{x,r}^S (A_1 A_2) - k_{x,m}^A k_{y,s}^S (B_1 B_2) \quad (\text{A.16})$$

If  $\vec{e}_l^A$  *TM* and  $\vec{e}_p^{s,1}$  *TE*, inner-product  $D_{lp}^{z=0}$  results in

$$D_{lp}^{z=0, TM \bullet TE} = \int_0^{b/2} \int_0^{a/2} \vec{e}_l^A \cdot \vec{e}_p^{s,1} dx dy = k_{x,r}^A k_{y,n}^s (A_1 A_2) - k_{y,s}^A k_{x,m}^s (B_1 B_2) \quad (\text{A.17})$$

If both  $\vec{e}_l^A$  and  $\vec{e}_p^{s,1}$  are *TM*, inner-product  $D_{lp}^{z=0}$  results in

$$D_{lp}^{z=0, TM \bullet TM} = \int_0^{b/2} \int_0^{a/2} \vec{e}_l^A \cdot \vec{e}_p^{s,1} dx dy = k_{x,r}^A k_{x,r}^s (A_1 A_2) + k_{y,s}^A k_{y,s}^s (B_1 B_2) \quad (\text{A.18})$$

The solution to each combination of  $D_{lp}^{z=d_N}$  is almost identical to the respective solution for  $D_{lp}^{z=0}$  with the only difference being in the terms  $\gamma_p^{s,1}$  and  $\mu_1$ . For example,  $\gamma_p^{s,N}$  and  $\mu_N$ , which are the propagation constant and permeability of the  $N^{\text{th}}$  layer (see Figure 3.2), will be used in the solution for  $D_{lp}^{z=d_N}$  versus  $\gamma_p^{s,1}$  and  $\mu_1$ . As such, the identities (i.e.  $A_1, A_2, B_1$ , and  $B_2$ ) provided for  $D_{lp}^{z=0}$  are again used for  $D_{lp}^{z=d_N}$ .

### **A.6 Proof for $F_{lp}$**

For the inner-product represented by  $F_{lp}$ , there are also four possible combinations of inner-products. Before the results are provided for the four mode combinations, there is another set of identities derived to make the answers more manageable. Therefore, let

$$A_1 = \int_0^{t/2} \sin(k_{x,m}^S x) \sin(k_{x,m}^A x) dx =$$

$$\begin{cases} \frac{t}{4} & \dots \text{for } k_{x,m}^S = k_{x,m}^A \\ \frac{\sin\left[\left(k_{x,m}^S - k_{x,m}^A\right)\frac{t}{2}\right]}{2\left(k_{x,m}^S - k_{x,m}^A\right)} + \frac{\sin\left[\left(k_{x,m}^S + k_{x,m}^A\right)\frac{t}{2}\right]}{2\left(k_{x,m}^S + k_{x,m}^A\right)} & \dots \text{for } k_{x,m}^S \neq k_{x,m}^A \end{cases}$$

$$A_2 = \int_0^{h/2} \sin(k_{y,n}^S y) \sin(k_{y,n}^A y) dy =$$

$$\begin{cases} 0 & \dots k_{y,n}^S = 0, \text{ or } k_{y,n}^A = 0 \\ \frac{h}{4} & \dots k_{y,n}^S = k_{y,n}^A \neq 0 \\ \frac{\sin\left[\left(k_{y,n}^S - k_{y,n}^A\right)\frac{h}{2}\right]}{2\left(k_{y,n}^S - k_{y,n}^A\right)} - \frac{\sin\left[\left(k_{y,n}^S + k_{y,n}^A\right)\frac{h}{2}\right]}{2\left(k_{y,n}^S + k_{y,n}^A\right)} & \dots k_{y,n}^S \neq k_{y,n}^A \end{cases}$$

$$B_1 = \int_0^{t/2} \cos(k_{x,m}^S x) \cos(k_{x,m}^A x) dx =$$

$$\begin{cases} \frac{t}{4} & \dots \text{for } k_{x,m}^S = k_{x,m}^A \\ \frac{\sin\left[\left(k_{x,m}^S - k_{x,m}^A\right)\frac{t}{2}\right]}{2\left(k_{x,m}^S - k_{x,m}^A\right)} + \frac{\sin\left[\left(k_{x,m}^S + k_{x,m}^A\right)\frac{t}{2}\right]}{2\left(k_{x,m}^S + k_{x,m}^A\right)} & \dots \text{for } k_{x,m}^S \neq k_{x,m}^A \end{cases}$$

$$B_2 = \int_0^{h/2} \cos(k_{y,n'}^S y) \cos(k_{y,n}^A y) dy = \begin{cases} 0 & \dots k_{y,n}^S = 0 \\ \frac{h}{4} & \dots k_{y,n'}^S = k_{y,n}^A \neq 0 \\ \frac{h}{2} & \dots k_{y,n'}^S = k_{y,n}^A = 0 \\ \frac{\sin\left[\left(k_{y,n'}^S - k_{y,n}^A\right)\frac{h}{2}\right]}{2\left(k_{y,n'}^S - k_{y,n}^A\right)} + \frac{\sin\left[\left(k_{y,n'}^S + k_{y,n}^A\right)\frac{h}{2}\right]}{2\left(k_{y,n'}^S + k_{y,n}^A\right)} & \dots \text{otherwise} \end{cases}$$

Although the identities were derived for the *TE-TE* case, they are compatible for the other three cases (i.e. *TE-TM*, *TM-TE*, and *TM-TM*). If both  $\vec{h}_l^s$  and  $\vec{h}_p^A$  are *TE*, the inner-product  $F_{lp}$  results in

$$F_{lp}^{TE \bullet TE} = Z_{TM,l}^{s,i} \int_0^{h/2} \int_0^{w/2} \vec{h}_l^s \cdot \vec{h}_p^A dx dy = \frac{k_{x,m}^s k_{x,m}^A (B_1 B_2) + k_{y,n}^s k_{y,n}^A (A_1 A_2)}{Z_{TE,p}^A} \quad (\text{A.19})$$

If  $\vec{h}_l^s$  *TE* and  $\vec{h}_p^A$  *TM*, inner-product  $F_{lp}$  results in

$$F_{lp}^{TE \bullet TM} = Z_{TM,l}^{s,i} \int_0^{h/2} \int_0^{w/2} \vec{h}_l^s \cdot \vec{h}_p^A dx dy = \frac{k_{y,n}^s k_{x,r}^A (A_1 A_2) - k_{x,m}^s k_{y,s}^A (B_1 B_2)}{Z_{TM,p}^A} \quad (\text{A.20})$$

If  $\vec{h}_l^s$  *TM* and  $\vec{h}_p^A$  *TE*, inner-product  $F_{lp}$  results in

$$F_{lp}^{TM \bullet TE} = Z_{TM,l}^{s,i} \int_0^{h/2} \int_0^{w/2} \vec{h}_l^s \cdot \vec{h}_p^A dx dy = \frac{k_{x,r}^s k_{y,n}^A (A_1 A_2) - k_{y,s}^s k_{x,m}^A (B_1 B_2)}{Z_{TE,p}^A} \quad (\text{A.21})$$

If both  $\vec{h}_l^s$  and  $\vec{h}_p^A$  are *TM*, inner-product  $F_{lp}$  results in

$$F_{lp}^{TM \bullet TM} = Z_{TM,l}^{s,i} \int_0^{h/2} \int_0^{w/2} \vec{h}_l^s \cdot \vec{h}_p^A dx dy = \frac{k_{y,s}^s k_{y,s}^A (B_1 B_2) + k_{x,r}^s k_{x,r}^A (A_1 A_2)}{Z_{TM,p}^A} \quad (\text{A.22})$$



Appendix A	Proofs of Inner-Products	A-1
A.1	Proof for $C_{lp}$	A-1
A.2	Proof for $C_{ll}$	A-2
A.3	Proof for $Q_{lp}$	A-2
A.4	Proof for $P_{lp}$	A-4
A.5	Proof for $D_{lp}$	A-5
A.6	Proof for $F_{lp}$	A-7

## Appendix B Sample Holder Drawings

Reducing the waveguide's cross sectional area by “ $P$ ” percent was accomplished by selecting an aperture having the same aspect ratio as the feed waveguide, centered on the cross-sectional axes of the feed waveguide (see Figure B-1), and having a cross-sectional area equal to  $P\%$  of the feed waveguide. Based on these criteria, the sample holder's aperture dimensions were calculated using (B.1) and (B.2).

$$h = b\sqrt{1-P} \quad (\text{B.1})$$

$$w = a\sqrt{1-P} \quad (\text{B.2})$$

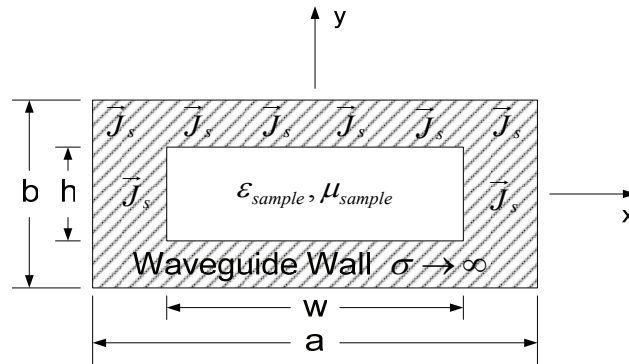
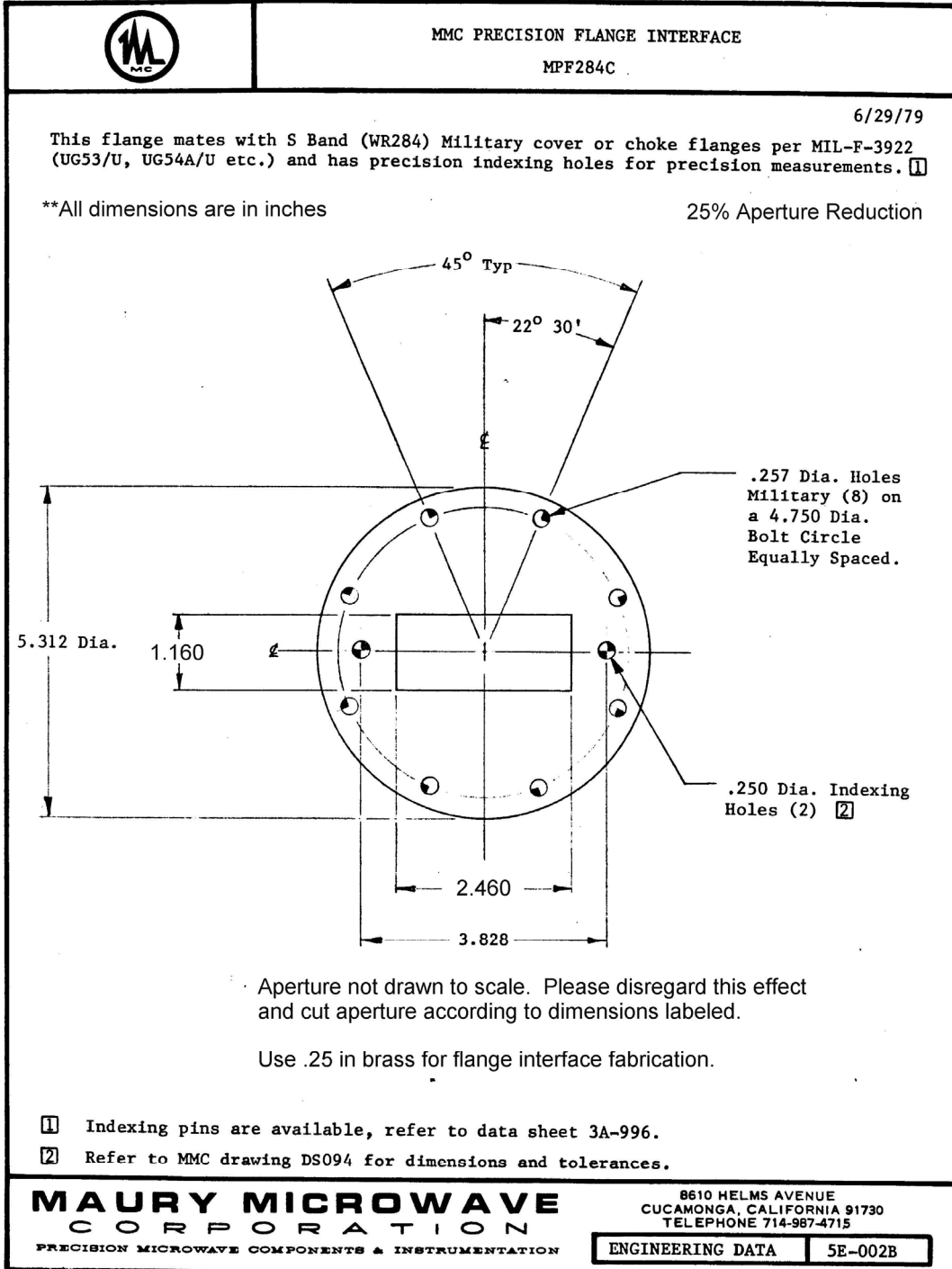
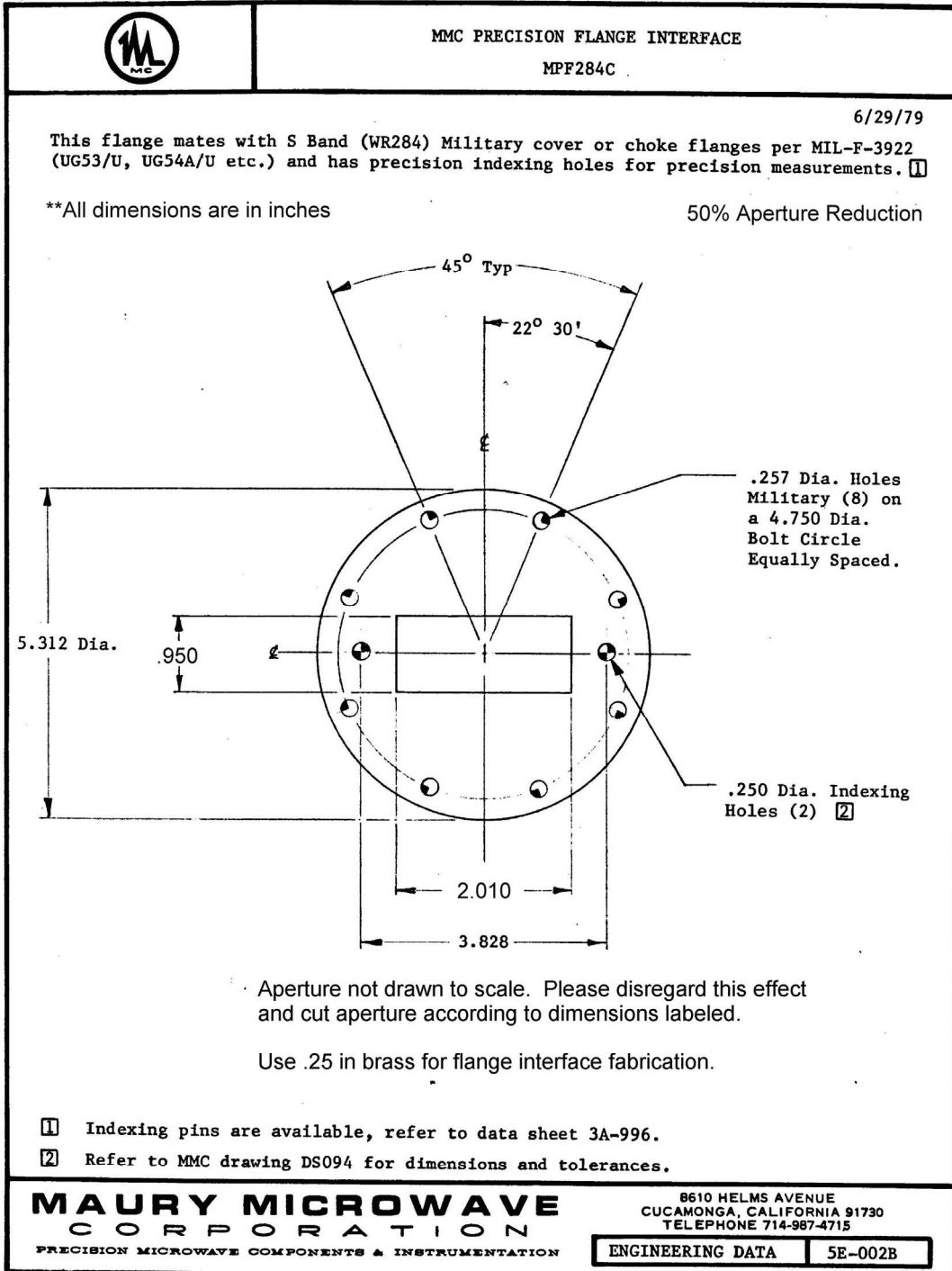


**Figure B-1** Cross-sectional view of 2-D stepped waveguide aperture

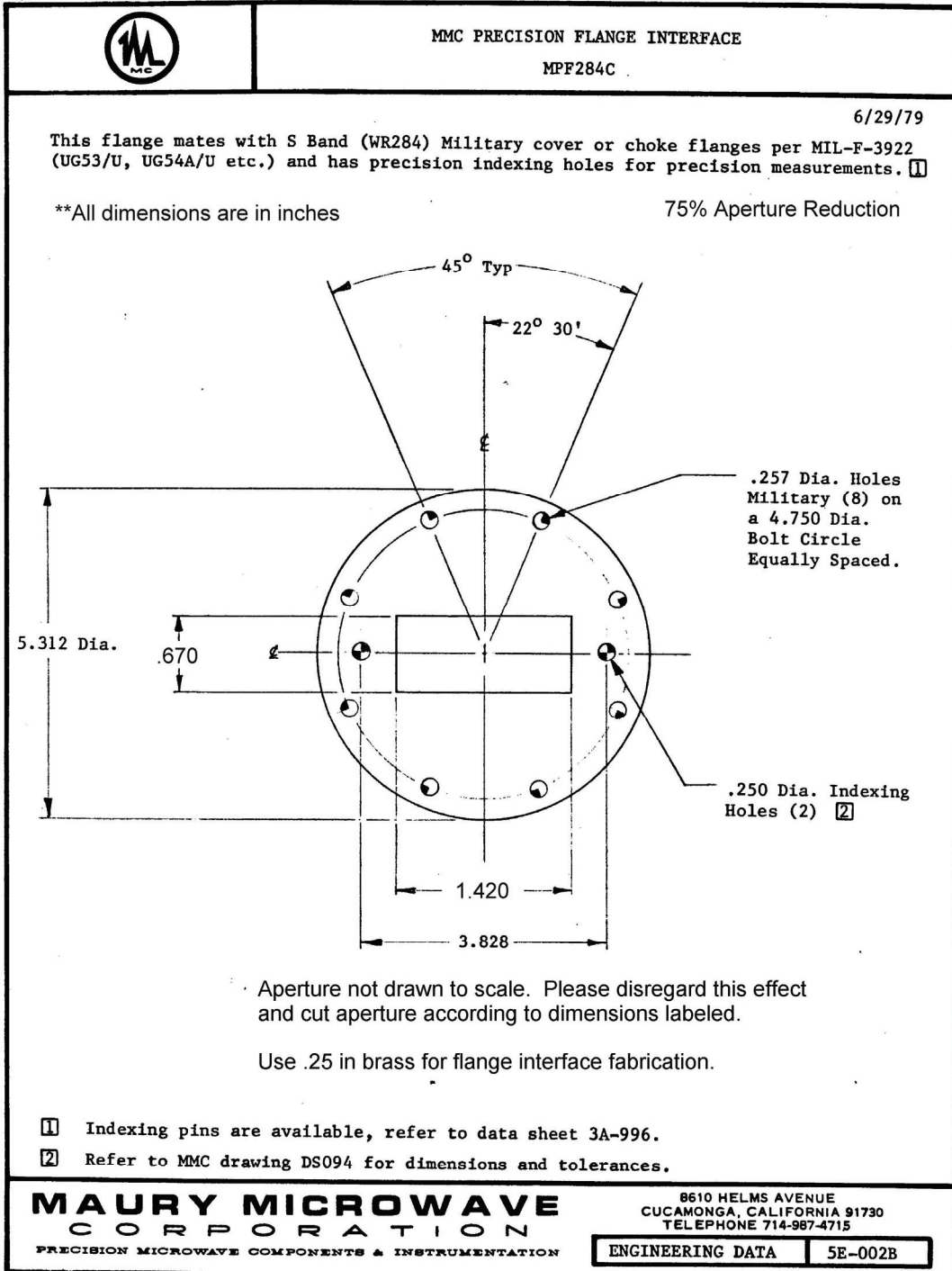
**B.1 25% Waveguide Reduction Sample Holder/Flange**



B.2 50% Waveguide Reduction Sample Holder/Flange



B.3 75% Waveguide Reduction Sample Holder/Flange



#### *B.4 Other Equipment*

<b><u>Description</u></b>	<b><u>Model Number</u></b>
Hewlett-Packard Network Analyzer	HP8510B
Hewlett-Packard S-Parameter Test Set	HP8515A
Maury Microwave Waveguide Calibration Kit	S7007H Option 14

Appendix B Sample Holder Drawings..... B-1

- B.1 25% Waveguide Reduction Sample Holder/Flange..... B-2
- B.2 50% Waveguide Reduction Sample Holder/Flange..... B-3
- B.3 75% Waveguide Reduction Sample Holder/Flange..... B-4
- B.4 Other Equipment ..... B-5

Figure B-1 Cross-sectional view of 2-D stepped waveguide aperture ..... B-1

<b>REPORT DOCUMENTATION PAGE</b>				<i>Form Approved OMB No. 074-0188</i>	
<p>The public reporting burden for this collection of information is estimated to average 1 hour per response, including the time for reviewing instructions, searching existing data sources, gathering and maintaining the data needed, and completing and reviewing the collection of information. Send comments regarding this burden estimate or any other aspect of the collection of information, including suggestions for reducing this burden to Department of Defense, Washington Headquarters Services, Directorate for Information Operations and Reports (0704-0188), 1215 Jefferson Davis Highway, Suite 1204, Arlington, VA 22202-4302. Respondents should be aware that notwithstanding any other provision of law, no person shall be subject to a penalty for failing to comply with a collection of information if it does not display a currently valid OMB control number.</p> <p><b>PLEASE DO NOT RETURN YOUR FORM TO THE ABOVE ADDRESS.</b></p>					
<b>1. REPORT DATE (DD-MM-YYYY)</b> 03-21-2005		<b>2. REPORT TYPE</b> Master's Thesis		<b>3. DATES COVERED (From - To)</b> Aug 2003 - Mar 2005	
<b>4. TITLE AND SUBTITLE</b>  Efficient Electromagnetic Material Characterization Via 2-D Rectangular Waveguide Reduction				<b>5a. CONTRACT NUMBER</b>	
				<b>5b. GRANT NUMBER</b>	
				<b>5c. PROGRAM ELEMENT NUMBER</b>	
				<b>5d. PROJECT NUMBER</b>	
<b>5. AUTHOR (S)</b> Dwyer, Derek, R., 1Lt, USAF				<b>5e. TASK NUMBER</b>	
				<b>5f. WORK UNIT NUMBER</b>	
<b>7. PERFORMING ORGANIZATION NAMES(S) AND ADDRESS(S)</b> Air Force Institute of Technology Graduate School of Engineering and Management (AFIT/EN) 2950 Hobson Way; Bldg 641 WPAFB OH 45433-7765				<b>8. PERFORMING ORGANIZATION REPORT NUMBER</b>  AFIT/GE/ENG/05-01	
<b>9. SPONSORING/MONITORING AGENCY NAME(S) AND ADDRESS(ES)</b> AFRL/SNS(AFMC) Attn: George R. (Bob) Simpson, Ph.D. 2591 K Street; Bldg 254 WPAFB, OH 45433-7602 (937) 255-9288 (george.simpson@wpafb.af.mil)				<b>10. SPONSOR/MONITOR'S ACRONYM(S)</b>	
				<b>11. SPONSOR/MONITOR'S REPORT NUMBER(S)</b>	
<b>12. DISTRIBUTION/AVAILABILITY STATEMENT</b> Approved for Public Release; Distribution Unlimited					
<b>13. SUPPLEMENTARY NOTES</b>					
<b>14. ABSTRACT</b> A new, low-frequency, rectangular waveguide-based electromagnetic material characterization technique is developed that will reduce the test sample size in two dimensions realizing up to 50 percent reduction in sample cross-sectional area. To achieve this, custom made, reduced aperture, sample holder flanges were used that reduce the waveguide's excessive cross-sectional dimensions, resulting in reduced sample fabrication costs. Additionally, MatLab® code was developed to implement the rigorously derived modal-analysis solution that accommodates induced, higher-order transverse electric and transverse magnetic modes and accurately extract the reduced test sample's constitutive parameters. Experimental results using various test samples are compared to known, full-aperture measurements for both the reduced aperture waveguide configurations to verify the theoretical analysis. A differential error analysis is also performed for each configuration in an attempt to estimate the error associated with test sample thickness, aperture dimensions, and sample placement uncertainties.					
<b>15. SUBJECT TERMS</b> Waveguide Irises (BT), Electromagnetic Properties (NT), Modal-Analysis (BT)					
<b>16. SECURITY CLASSIFICATION OF:</b>			<b>17. LIMITATION OF ABSTRACT</b>  UU	<b>18. NUMBER OF PAGES</b>  93	<b>19a. NAME OF RESPONSIBLE PERSON</b> Dr Michael J Havrilla
REPORT U	ABSTRACT U	c. THIS PAGE U			<b>19b. TELEPHONE NUMBER (Include area code)</b> (937) 255-3636 x-4582 (michael.havrilla@afit.edu)